



AFRL-AFOSR-VA-TR-2016-0339

---

Enhanced convection heat transfer using small-scale vorticity concentrations effected by flow-driven, aeroelastically vibrating reeds

ARI GLEZER  
GEORGIA TECH RESEARCH CORPORATION

---

08/03/2016  
Final Report

DISTRIBUTION A: Distribution approved for public release.

Air Force Research Laboratory  
AF Office Of Scientific Research (AFOSR)/ RTA1  
Arlington, Virginia 22203  
Air Force Materiel Command

<b>REPORT DOCUMENTATION PAGE</b>				<i>Form Approved OMB No. 0704-0188</i>	
<small>The public reporting burden for this collection of information is estimated to average 1 hour per response, including the time for reviewing instructions, searching existing data sources, gathering and maintaining the data needed, and completing and reviewing the collection of information. Send comments regarding this burden estimate or any other aspect of this collection of information, including suggestions for reducing the burden, to Department of Defense, Washington Headquarters Services, Directorate for Information Operations and Reports (0704-0188), 1215 Jefferson Davis Highway, Suite 1204, Arlington, VA 22202-4302. Respondents should be aware that notwithstanding any other provision of law, no person shall be subject to any penalty for failing to comply with a collection of information if it does not display a currently valid OMB control number.</small>					
<b>PLEASE DO NOT RETURN YOUR FORM TO THE ABOVE ADDRESS.</b>					
<b>1. REPORT DATE (DD-MM-YYYY)</b>		<b>2. REPORT TYPE</b>		<b>3. DATES COVERED (From - To)</b>	
<b>4. TITLE AND SUBTITLE</b>				<b>5a. CONTRACT NUMBER</b>	
				<b>5b. GRANT NUMBER</b>	
				<b>5c. PROGRAM ELEMENT NUMBER</b>	
<b>6. AUTHOR(S)</b>				<b>5d. PROJECT NUMBER</b>	
				<b>5e. TASK NUMBER</b>	
				<b>5f. WORK UNIT NUMBER</b>	
<b>7. PERFORMING ORGANIZATION NAME(S) AND ADDRESS(ES)</b>				<b>8. PERFORMING ORGANIZATION REPORT NUMBER</b>	
<b>9. SPONSORING/MONITORING AGENCY NAME(S) AND ADDRESS(ES)</b>				<b>10. SPONSOR/MONITOR'S ACRONYM(S)</b>	
				<b>11. SPONSOR/MONITOR'S REPORT NUMBER(S)</b>	
<b>12. DISTRIBUTION/AVAILABILITY STATEMENT</b>					
<b>13. SUPPLEMENTARY NOTES</b>					
<b>14. ABSTRACT</b>					
<b>15. SUBJECT TERMS</b>					
<b>16. SECURITY CLASSIFICATION OF:</b>			<b>17. LIMITATION OF ABSTRACT</b>	<b>18. NUMBER OF PAGES</b>	<b>19a. NAME OF RESPONSIBLE PERSON</b>
<b>a. REPORT</b>	<b>b. ABSTRACT</b>	<b>c. THIS PAGE</b>			<b>19b. TELEPHONE NUMBER (Include area code)</b>

## I. OVERVIEW AND OBJECTIVES

The Georgia Institute of Technology, the Johns Hopkins University, and the University of Michigan collaborated on a three-year integrated experimental, modeling, and numerical research program that focused on overcoming the limits of forced convection heat transport from conventional air-side heat exchangers by exploiting novel flow, structure, and heat transfer interactions. Heat transfer at the surface and in the bulk stream is enhanced by the formation and advection of a hierarchy of vortical motions, to overcome inefficiencies of current air cooling systems in which the volume flow rate is the primary control parameter. A unique element of the proposed work is the production of small vortices near the heated surfaces by *harnessing mechanical energy from the embedding flow to drive aeroelastic flutter of simple self-oscillating reeds* (Figure I-1).

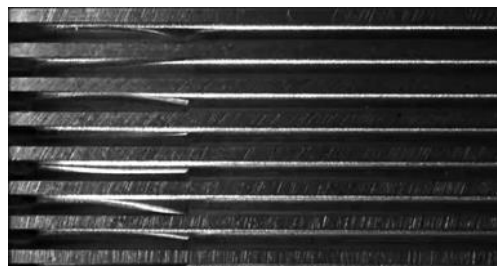


**Figure I-1** Self-oscillating reeds within 2.5 mm wide heat sink channels.

**Motivation** Thermal management has become a major limiting challenge for current and future military air vehicles where high heat flux cooling requirements are coupled with a limited payload capacity. Among thermal management challenges in several systems, the USAF Scientific Advisory Board identified high-temperature aircraft power control and conversion electronics and electromechanical actuators (EMAs) among the top-ten technology solutions that are critical for meeting the near-, mid-, and far-term thermal management needs of Air Force platforms (SAB-TR-07-05-NP, 2007). While high-efficiency air cooling systems can provide an attractive alternative for thermal management of high-power flight platforms, in most cases, these systems operate at low Reynolds numbers to minimize flow losses and cooling power at the cost of nearly-laminar, and therefore less effective, heat transfer.

**Objectives** The investigations under this AFOSR Program focused on the development of the fundamental knowledge needed to implement, design, and optimize the use of aeroelastically-driven self-oscillating reeds for improving the heat transfer characteristics within high-aspect-ratio channels of air-side heat exchangers. Using experiments as well as computational models (inviscid and viscous), the research program explored the interactions between the flow, reed and thermal field, and characterized the effects of the reeds on heat transfer within the Reynolds number regime  $10^2 < Re_c < 10^4$ . Specific emphasis was placed on the controlled production of small-scale vortices, their advection into and interactions with the boundary layer of the heated surface, and their role in enhancing heat convection from the surface and thermal transport. The flow is 3-D, vortex-dominated and transitional, with complex flow-structure dynamics over a broad range of scales. Of particular interest are fluid/structure dynamical interactions, and the topology of and advection of the induced vorticity concentrations.

It is anticipated that the ability to control enhancement of heat transfer at relatively low air flow rates will enable the development of compact heat sinks with transformative reductions in thermal resistance, power consumption, weight, and volume, that supports compact electronics and electric and electromechanical systems in military as well as commercial aircraft.

## II. THERMAL MANAGEMENT USING DIRECT SMALL-SCALE ACTUATION

**The Thermal Challenge** A major challenge in the design and packaging of high-performance electronic systems, such as high-speed microprocessors, power converters, micro- and millimeter-

wave power electronics, optoelectronics, etc., is the demand for high-power-density heat dissipation to ensure proper operation and to prevent thermal damage. For instance, Zerby & Kuszewski (2002) projected die cooling fluxes as high as  $1000 \text{ W/cm}^2$ . Proper thermal management at these large power densities requires designers to consider new approaches and technologies for enhanced heat transfer. In particular, in recent years, thermal management has become a major limiting challenge for current and future military air vehicles where high power and high heat flux cooling requirements, are coupled with a limited payload capacity (e.g., Mahefkey et al., 2004). Among thermal management challenges in several systems, the USAF Scientific Advisory Board identified high-temperature aircraft power control and conversion electronics and electromechanical actuators (EMAs) among the top-ten technology solutions that are critical for meeting the near-, mid-, and far-term thermal management needs of Air Force platforms (SAB-TR-07-05-NP, 2007). While the replacement of hydraulic systems in current aircraft designs with electromechanical actuators will undoubtedly lead to significant reductions in weight and complexity, and increase endurance, reliability and aircraft survivability, it will also necessitate installation of effective cooling systems. Although current limitations of conventional air cooling systems may suggest the use of liquid cooling (e.g., Agostini *et al.* 2007), the added weight and complexity can offset the benefits from elimination of the hydraulic system.

**Current State of the Art** High-efficiency air cooling systems can provide an attractive alternative for thermal management of high-power electronic hardware on military and commercial air vehicles. Several investigations have already demonstrated state-of-the-art compact, air-cooled heat sinks for dissipation up to 300W, *however, it is remarkable that in most current applications, these heat sinks are designed to operate at low characteristic channel Reynolds numbers  $Re_c < 3,000$*  so as to minimize flow losses and cooling power; this however, comes at the cost of nearly-laminar, and therefore less effective heat transfer. As an example of design methodology for optimization of air-cooled plate-fin heat sinks, (Bar-Cohen et al., 2002) demonstrated power dissipation of up to 370W using a  $0.1 \times 0.1 \text{ m}$  footprint heat sink operating at  $Re_c < 1,500$ . Similar observations were made by Xu et al. (2004, 250W  $Re_c \approx 1,000$ ), and by Drofenik et al. (2005, 300W,  $800 < Re_c < 1,300$ ).

Forced convection heat transfer within the high aspect-ratio channels formed by heat sink fins is typically limited by the available air volume flow-rate. This limitation is manifested by two closely-coupled stages of heat transport. First, the local heat transfer rate from the fin surface (with area  $A$ ) to the adjacent air flow  $Q = h \cdot A \cdot \Delta T_w$  is limited by the heat transfer coefficient  $h$  and the temperature difference between the local air stream and the fin surface  $\Delta T_w$ . Second, the overall heat transport for a given mass flow rate  $\dot{m}$ ,  $Q = \dot{m} \cdot C_p \cdot \Delta T_a$  depends on the temperature rise of the air  $\Delta T_a$  ( $C_p$  is the specific heat). Both the local and global heat transport rates can be drastically enhanced by unsteady flow fluctuations and mixing as the Reynolds number and flow rate increase (e.g., Incropera et al., 2007), or, alternatively, by deliberate introduction of secondary vortices using surface-mounted vortex generators (e.g., Tiggelbeck et al., 1991, Biswas et al., 1996, Tanaka et al., 2003). However, both approaches lead to a significant increase in the flow losses, thereby limiting the coefficient of performance (COP) which measures the ratio of thermal power dissipated to the fluid power invested in heat removal.

**Small-Scale Heat Transfer:** A new approach for effecting small-scale flow motions and mixing by direct actuation of dissipative scales in free and wall-bounded shear flows was developed at Georgia Tech by Glezer and his co-workers (Wiltse and Glezer, 1998, Vukasinovic et al., 2010). In this approach, the characteristics of low- $Re_c$  flows can be significantly altered by deliberate

forcing of small-scale vortical structures having characteristic wavelengths that are typically an order of magnitude or more smaller than the relevant local or global length scale of the baseline flow. *An important attribute of this approach is that in comparison to passive vortex generators it can be applied with minimal penalty in terms of flow losses.* The formation and advection of these small-scale, unsteady vortical motions engendered by a synthetic jet actuator was used by Gillespie et al. (2006) to enhance thermal transport from heated surfaces by increasing both the heat transfer at the surface and cross-stream mixing. The work at Georgia Tech has also demonstrated that synthetic jets can replace the fans on conventional heat sinks by forcing the small-scale fluidic motions induced by the jets within the high-aspect ratio fin channels of the heat sinks. *Direct actuation of small-scale motions within the heat sink channels leads to significant improvement in their thermal performance at significantly lower flow rates than are needed from the system fan* (e.g., Mahalingam and Glezer, 2005, and Gerlach et al., 2009). Building on these ideas, Hidalgo et al. (2010) demonstrated a novel approach to enhanced cooling of fan-driven heat sinks *without increasing the heat sink's characteristically low Reynolds number* by using deliberate, time-periodic shedding of small-scale vortices that are induced by the vibration of ultra-thin, planar piezoelectrically-driven reeds that span the width of the heat sink channels. Their approach paved the way to the investigations under the present program.

### III. TECHNICAL REPORT

#### III.1. Analytical Methods

##### III.1.1 Inviscid Modeling of Aeroelastic Vibrating Plates

The flutter instability has been a major topic in the field of fluid-structure interactions for many years (Theodorsen, 1935, von Kármán & Burgers, 1935, Glauert, 1947, Shelley & Zhang, 2011). When a flexible body is aligned with a steady fluid flow, it becomes unstable to transverse oscillations. Alben & Shelley (2008) modeled the dynamics using a nonlinear beam equation in one space dimension under the pressure forcing of a two-dimensional inviscid flow. Because the flow is inviscid, the body supports a singular “bound” vortex sheet that is advected off of the trailing edge, becoming a “free” vortex sheet which in the absence of viscosity becomes one-dimensional curvilinear vortex. The flux of vorticity into the wake is set by the Kutta condition (Crighton, 1985) at the trailing edge. The equations for the coupled flow-body system of a flag (Alben, 2009a) are evolved using an implicit scheme which includes an iterative Newton-type method. In previous work on the shedding of vortex sheets from sharp-edged bodies (Krasny, 1991, Nitsche & Krasny, 1994, Jones, 2003, Shukla & Eldredge 2007), the body motion was prescribed (not coupled to the fluid forces). The first numerical method for the fully-coupled problem was presented by Alben (2009a). Several recent studies have calculated the linear stability boundary in a two-parameter space using small-amplitude equations (Eloy et al., 2007, Alben, 2008, Shelley & Zhang 2011). This work was extended to include channel walls (Doaré et al. 2011), but the walls confine the flow primarily in the spanwise direction, not the flapping direction, which was the main interest of the present program. Alben’s model (2009a) was used to consider large-amplitude reed and vortex-wake dynamics in a channel for which comparisons with viscous simulations (Alben (2009b) against Kim et al., 2010) validated the inviscid model assumption that vortex shedding is mainly confined to the trailing edge.

##### III.1.2 Inviscid Reed Modeling

A reed can enhance heat transfer by altering the channel flow through its vortex wake, inducing flow separation from the channel walls and increasing stirring throughout the channel. The physical parameter space of such a system is large, so an important goal of this work was to characterize the reed stability and reed and vortex wake dynamics within a reduced model, which neglects viscosity and 3D effects.

We consider an inviscid model for a thin plate or reed oscillating in a flow. An example of a reed and vortex wake in a channel are shown in Figure III.1.1 (a). The channel is the region  $A < y < H - A$ . The reed is shown as a thick black line with leading edge at the origin. The vortex wake is the thinner black line that emanates from the trailing edge of the reed and forms spirals as it evolves downstream of the reed. A uniform horizontal flow with velocity  $U$  has been applied at infinity upstream, and the reed, wake, and flow evolve under the following set of equations: Euler's equations of fluid momentum balance; the no-penetration condition on the reed; a mechanical force balance between reed bending rigidity, inertia, and fluid pressure; Kelvin's Circulation theorem; the Birkhoff-Rott equation for free vortex sheet dynamics; and the Kutta condition governing vorticity production at the reed's trailing edge.

We also consider a simplified problem for which analytical stability results can be obtained. We replace the finite reed with an infinite reed, extending upstream and downstream. An example of the infinite reed in a channel (thick black line) and image system of reeds (gray lines) is shown in Figure III.1.1 (b). For small deflections, we can linearize the model equations about the

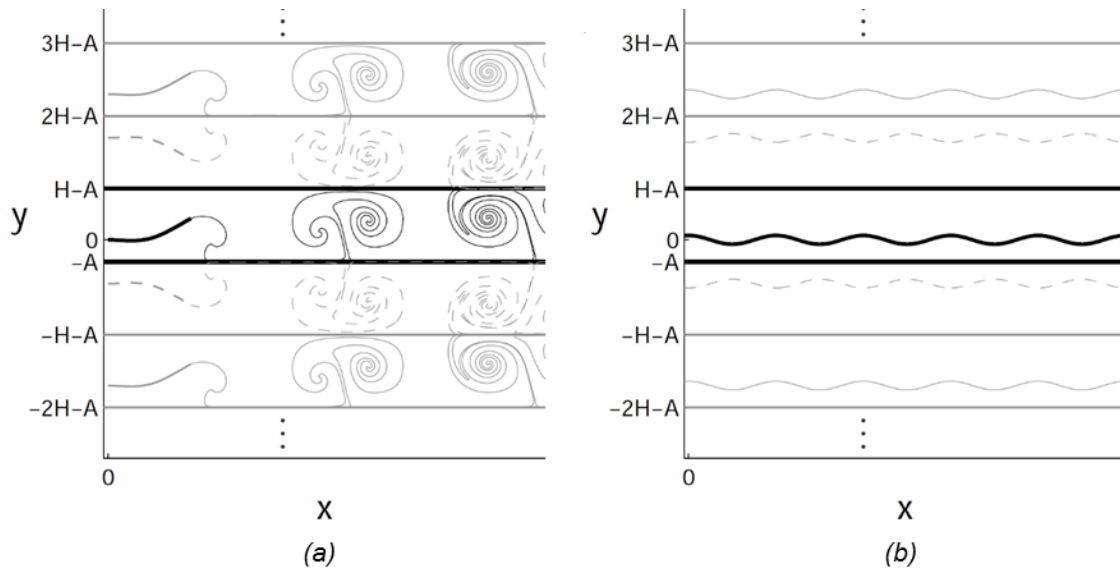


**Figure III.1-1.** Examples of image systems of reeds and vortex wakes that impose no-penetration boundary conditions on the channel walls at  $y = -A$  and  $H-A$ . a) A reed (thick black line emanating from the origin) and vortex wake (thin black line emanating from the reed's trailing edge) are shown with their images (solid and dashed gray lines). b) For the infinite reed case, a sinusoidal body is shown (thick black line) with images (solid and dashed gray lines).

horizontal-reed-in-a-uniform-flow state. The linearized equations have solutions which are complex exponentials in space and time and give a dispersion relation which determines when a perturbation of a given wavenumber is unstable.

### III.1.3 Finite Reed Results: Stability Boundaries

We compute the stability boundaries for the finite reed in the  $R_1$ - $R_2$  plane. We compute the growth (or decay) rates of an initial perturbation on a 33-by-33 grid of values in  $R_1$ - $R_2$  space spanning several decades in each parameter. We interpolate these values to find the location of the line with zero growth rate, which is the stability boundary. We compute the stability boundaries for two different values of  $A/H$ , 0.01 (shown in Figure III.1.2a), for which the far wall is 99 times as distant as the near wall, and 0.5 (shown in Figure III.1.2 (b)), for a symmetric channel. In each panel, the stability boundaries are given for twelve different values of near-wall-distance ( $A/L$ ) ranging from 0.005 to 5 (labeled), and plotted with different shades of gray and line thicknesses.

For the larger  $A/L$  (1.5, 2.5, and 5), we find good convergence to the stability boundary for the unbounded case in panels (a) and (b). As  $A/L$  decreases, the "plateau" portion of the stability boundary moves upwards, towards larger  $R_1$  and  $R_2$ , and becomes more curved. At smaller  $R_2$ , the stability boundary shifts slightly rightward, towards larger  $R_1$ , mainly at very small values of  $A/L$ . The main difference between panels (a) and (b) is that the shifts are somewhat greater in panel (b), consistent with an increased instability due to increased confinement.

### III.1.4 Large-Amplitude Dynamics

We describe how some of the basic quantities of the flapping state---amplitude, frequency, and number of deflection extrema---vary with the channel confinement parameter  $A/L$ , across  $R_1$  and  $R_2$ . In all of the results presented here, the reed does not collide with or intersect the channel

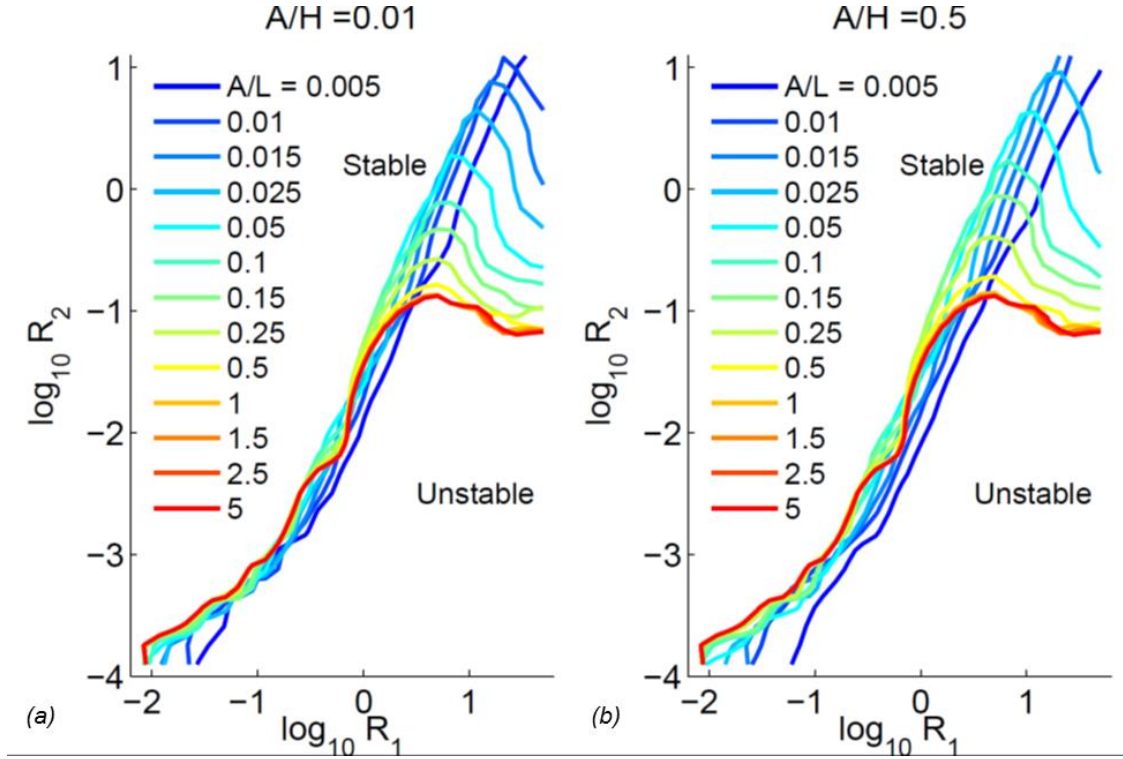


**Figure III.1.2.** Stability boundaries for finite flags in the space of dimensionless flag inertia ( $R_1$ ) and bending rigidity ( $R_2$ ). Boundaries are shown for various ratios of near-wall-distance to flag length  $A/L$  (labeled) when the far wall is much farther away ( $A/H = 0.01$ , panel a) and when the two walls are equidistant ( $A/H = 0.5$ , panel b).

walls at any time. In some computations, particularly for heavier, more flexible reeds (larger  $R_1$  and smaller  $R_2$ ), the reed does intersect the wall, at which the point the computation ends and the results are discarded. A special treatment would be needed to allow for contact during the dynamics, and we do not pursue this here.

First, we consider the symmetric channel ( $A/H = 0.5$ ). We identify a set of  $(R_1, R_2)$  which have a dominant flapping frequency across a wide range of  $A/L$ . These values of  $(R_1, R_2)$  are shown by circles in Figure III.1.3 (d). For each such  $(R_1, R_2)$ , we plot the flapping amplitude (Figure III.1.3 (a)), frequency (Figure III.1.3 (b)) and average number of extrema (Figure III.1.3 (c)). In each of the panels (a)-(c), values for a given  $(R_1, R_2)$  are a set of crosses connected by a solid line. We do not label each line by its value of  $(R_1, R_2)$  to prevent visual clutter, and also because we are mainly interested in the trends which are common across the set of plots. First, we consider the flapping amplitude (panel a). For most values of  $(R_1, R_2)$ , the behavior is as follows. Starting at the right side of the panel, where each line tends to its unbounded value at large  $A/L$ , we move to the left, in the direction of decreasing  $A/L$ , or decreasing channel width. In most cases the amplitudes are nearly unchanged (but with a slight increase, evidence of attraction to the walls) until  $A$  decreases to about the size of the amplitude in the unbounded case. Then the amplitude is less than  $A$ , since no wall contact occurs. In this regime, the amplitude is usually quite close to  $A$ , however. But in some cases it is significantly less, so the reed remains well away from the walls. Meanwhile, the frequency (panel b) increases as the walls move towards the reed. In several cases the increase occurs as a jump separating approximate "plateau" regions. These cases are plotted with thick gray lines in panel b, with  $(R_1,$



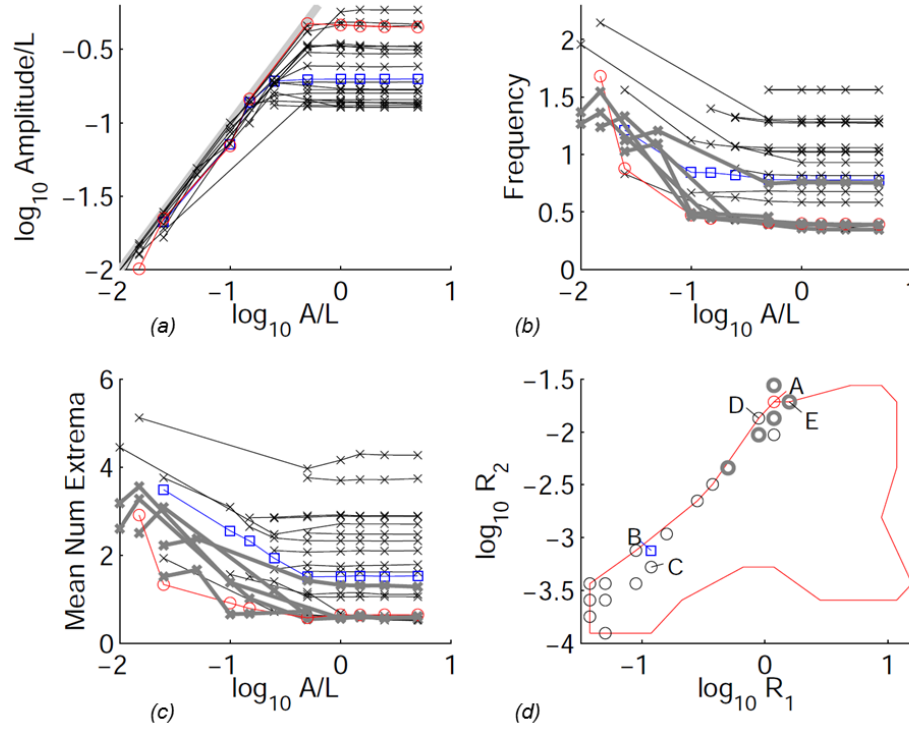


**Figure III.1.3.** Flapping amplitudes (a), dominant frequencies (b), and time-averaged numbers of extrema in reed deflection (c) for reeds in symmetric channels ( $A/H = 0.5$ ) with various wall spacings ( $A/L$ , shown on horizontal axes). The crosses connected by a given line correspond to a given  $(R_1, R_2)$  pair. These are not labeled individually but the ensemble of values is shown by circles (and other symbols) in panel (d). For five values with labels A-E, reed snapshots are shown in the panels of figure 4 with corresponding labels.

$R_2$ ) shown as thick gray circles in panel (d). As the frequency increases, so does the mean number of deflection extrema (panel c), showing that the reed adopts a "wavier" shape as the walls move inward. The thick gray lines correspond to those for the frequency (panel b), showing that the mean numbers of extrema also undergo jumps, and remain close to certain values over a range of  $A/L$ . In panel d, five  $(R_1, R_2)$  values are labeled with letters A-E. These refer to the panels in Figure III.1.4, in which we show sequences of snapshots at these selected  $(R_1, R_2)$  values.

### III.1.5 Flapping State Transitions

Figure III.1.4 (a) shows a typical sequence of flapping states as  $A/L$  decreases for fixed reed and flow parameters ( $R_1$  and  $R_2$ ). In each panel the flapping frequency is listed, denoted by  $F$ . First, at  $A/L = 5$ , the state is essentially the unbounded case. In the next frame (moving to the right),  $A/L = 0.5$ , so the walls are now quite close to the reed. The reed motion is nearly unchanged, however, with only a slight increase in amplitude. This slight "wall attraction" occurs at various  $(R_1, R_2)$ . Moving again to the right ( $A/L = 0.15$ ), the reed continues to flap with nearly the same shape, but with a much smaller amplitude, enforced by the walls. It is almost as though the flapping motion has simply been scaled down in the vertical direction. The flapping frequency is also nearly the same. In the next frame ( $A/L = 0.1$ ), the shape and frequency are again nearly the same, but the amplitude has decreased again. Interestingly, the reed is farther from the walls in a relative sense than in the previous panels, even though the degree of confinement is now greater.

Moving to the next panel ( $A/L = 0.025$ ), the reed finally undergoes a large change in shape and in frequency (which is nearly double the previous value). The reed has transitioned to a very different flapping state. Another large transition occurs in the next frame ( $A/L = 0.015$ ), where the frequency nearly doubles again and the number of extrema also increases. Relative to the channel width, the reed is now farther from the channel wall than in the previous panel. The data corresponding to case A are shown by red

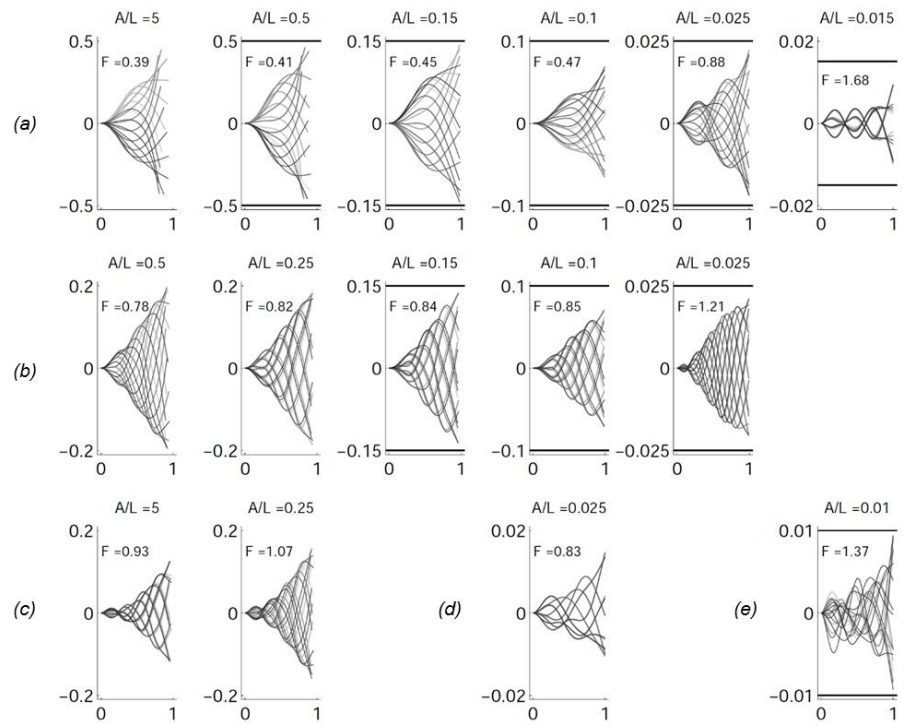


**Figure III.1.4.** Snapshots for flags with fixed values of  $R_1$  and  $R_2$  in symmetric channels ( $A/H = 0.5$ ) of varying half-width ( $A/L$ ). Each of the panels (a)-(e) corresponds to a different pair of  $R_1$  and  $R_2$ , labeled in figure 3D. Within each panel, a frame shows reed snapshots at a particular  $A/L$  (labeled). The axes have different scales. The dominant flapping frequencies are labeled  $F$ .

circles in the panels of Figure III.1.3. Moving to panel (b), the second row of Figure III.1.4,  $R_1$  and  $R_2$  (labeled '(b)' in Fig. 3d) are now reduced by about a factor of 10. In the unbounded state, similar to the first frame, the reed shows a higher bending mode than in panel (a), and a higher frequency. As  $A/L$  is decreased to 0.25, there is essentially no change in the flapping state. As  $A/L$  is decreased again to 0.15 and to 0.1, the flapping amplitude drops twice to fit within the successively smaller channels, but the reed shapes and frequencies are only slightly changed. In the last frame ( $A/L = 0.025$ ), the reed has moved to a higher bending mode with a higher frequency. The data corresponding to case B are shown by blue squares in the panels of Figure III.1.3. Panel (c) shows, at a nearby value of  $(R_1, R_2)$ , another example of the slight increase in flapping amplitude which can occur when the channel walls move closer to the reed. The first frame ( $A/L = 5$ ) is representative of the unbounded state. In the second ( $A/L = 0.25$ ), the walls are closer to the reed, and it has a small but noticeable increase in amplitude. Panel (d) shows an example of an asymmetric periodic state which occurs even though the channel is symmetric. Such asymmetric states are common in chaotic flapping, for which an example is shown in panel e, but are rare for periodic flapping in the symmetric channel.

### III.1.6 Concluding Remarks

- i Using nonlinear vortex-sheet simulations, we determined the region in parameter space in which a straight reed in a channel-bounded inviscid flow is unstable to flapping motions. We

found that for heavier reeds, greater confinement increases the size of the region of instability. For lighter reeds, confinement has little influence.

- ii* We then computed the stability boundaries analytically for an infinite reed, and found similar results.
- iii* For the finite reed we also considered the effect of channel walls on the large-amplitude periodic flapping dynamics. We found that multiple flapping states are possible but rare at a given set of parameters, when periodic flapping occurs. As the channel walls approach the reed, its flapping amplitude decreased roughly in proportion to the near-wall distance, for both symmetric and asymmetric channels. Meanwhile, its dominant flapping frequency and mean number of deflection extrema (or "wavenumber") increased in a nearly stepwise fashion. That is, they remained nearly unchanged over a wide range of channel spacing, but when the channel spacing was decreased below a certain value, they had sharp increases corresponding to a higher flapping mode.
- iv* The location of the reed stability boundary was similar for the inviscid model, viscous simulations, and the experiments. The flapping dynamics (reed mode shapes) were also similar at several points near the stability boundary.

## III.2 Computational Analysis

### III.2.1 Computational Modeling of Coupled Flow-Structure-Thermal (CFST) Dynamics

Assuming  $U$  denotes the characteristic velocity,  $L$  the characteristic length,  $T_s$  the temperature of boundaries and  $T_0$  the baseline temperature of the incoming flow temperature, the governing equations for incompressible flow and forced thermal convection can be written in their non-dimensional form as,

$$\frac{\partial \mathbf{u}}{\partial t} + \nabla \cdot (\mathbf{u}\mathbf{u}) = -\nabla p + \frac{1}{Re} \nabla^2 \mathbf{u} + \mathbf{f} \quad (\text{III.2.1})$$

$$\nabla \cdot \mathbf{u} = 0 \quad (\text{III.2.2})$$

$$\frac{\partial T}{\partial t} + \mathbf{u} \cdot \nabla T = \frac{1}{Re \cdot Pr} \nabla^2 T + \mathbf{q} \quad (\text{III.2.3})$$

The Lagrangian (reed) and Eulerian (momentum, temperature) variables are related together by the Dirac delta function based immersed boundary formulation. For example, the Lagrangian fluid velocity  $\mathbf{U}$ , and Lagrangian fluid temperature  $\Gamma$  at the position of the beam are obtained by,

$$\mathbf{U}(s, t) = \int_{\Omega_F} \mathbf{u}(\mathbf{x}, t) \delta[\mathbf{x} - \mathbf{X}(s, t)] d\mathbf{x} \quad (\text{III.2.4})$$

$$\Gamma(s, t) = \int_{\Omega_F} T(\mathbf{x}, t) \delta[\mathbf{x} - \mathbf{X}(s, t)] d\mathbf{x} \quad (\text{III.2.5})$$

where  $\Omega_F$  is the fluid domain. A similar relation is employed to relate the Lagrangian and Eulerian descriptions of force densities and heat sources, i.e.

$$\mathbf{f}(\mathbf{x}, t) = \int_{\Omega_S} \mathbf{F}(s, t) \delta[\mathbf{x} - \mathbf{X}(s, t)] ds \quad (\text{III.2.6})$$

$$\mathbf{q}(\mathbf{x}, t) = \int_{\Omega_S} \mathbf{Q}(s, t) \delta[\mathbf{x} - \mathbf{X}(s, t)] ds \quad (\text{III.2.7})$$

where  $\Omega_S$  is the domain of the immersed boundary (which in the case of the immersed reed is the contour along the reed).

The interaction between fluid variables and structural variables are calculated using a feedback law (Shoele and Mittal, 2012, Huang et al., 2007, Goldstein et al., 1993) as,

$$\mathbf{F}(s, t) = c_1 \int_0^t [\mathbf{U}(s, \tau) - \mathbf{V}(s, \tau)] d\tau + c_2 [\mathbf{U}(s, t) - \mathbf{V}(s, t)] \quad (\text{III.2.8})$$

$$\mathbf{Q}(s, t) = c_1 \int_0^t [\Gamma(s, \tau) - Y(s, \tau)] d\tau + c_2 [\Gamma(s, t) - Y(s, t)] \quad (\text{III.2.9})$$

where  $c_1$  and  $c_2$  are large penalty parameters to enforce no-slip and no-flux conditions along the reed. Furthermore,  $\mathbf{V}(s, t)$  and  $Y(s, t)$  are the velocity and temperature of the reed, respectively.

Finally, in the present study, it is assumed that because of the fluid lubrication, the reed does not actually collide but rather interact repulsively with the walls via a short-range repulsive force that can be formulated using the Dirac delta function where  $S_w$  is contour line along the walls, and  $k_c$

is the repulsive coefficient,

$$\mathbf{F}_c(s, t) = k_c \int_{s_w} \delta[\mathbf{x}(s') - \mathbf{X}(s, t)] \frac{\mathbf{x}(s') - \mathbf{X}(s, t)}{|\mathbf{x}(s') - \mathbf{X}(s, t)|} ds' \quad (\text{III.2.9})$$

This approach has successfully been used in previous studies (Pan et al., 2002, Uhlmann, 2005, Wang et al., 2008, Uddin et al., 2013, Maniyeri and Kang, 2014).

A finite-difference method is employed to solve the governing equations. A Crank-Nicolson scheme is used for implicitly advancing the diffusion terms, while all other terms, including convective terms are marched with the second-order Adams-Bashforth scheme. To summarize, the resulting formula for momentum equation is

$$\frac{u_i^{n+1} - u_i^n}{\Delta t} = \left( \frac{3}{2} H_i^n - \frac{1}{2} H_i^{n-1} \right) + G_i(p^{n+1}) + \frac{Gr}{Re^2} \hat{\mathbf{g}} T^{n+1} + \frac{1}{2} D(u_i^{n+1} - u_i^n) \quad (\text{III.2.10})$$

where  $H_i$  represents the  $i$ -th component of convective terms,  $G_i$  is the  $i$ -th component of the negative gradient operator divided by the fluid density,  $D$  is the diffusion operator divided by the density. The convective terms in the thermal convection equation is discretized with the SHARP scheme (Leonard, 1988). The central difference is applied for the diffusion terms and a four-step fractional-step time advancement scheme proposed by Choi and Moin (Choi and Moin, 1994) is used to solve Equation III.2.11. The interaction force between the reed and the fluid,  $\mathbf{F}^n$  is obtained explicitly from the Equation III.2.8 using the fluid and structural velocities up to the time step  $n$ ,

$$\mathbf{F}^n = c_1 \sum_{k=1}^n [\mathbf{U}^k - \mathbf{V}^k] \Delta t^k + c_2 [\mathbf{U}^n - \mathbf{V}^n] \quad (\text{III.2.11})$$

where  $\mathbf{V}^n$  is the velocity of the beam and  $\mathbf{U}^n$  is the fluid velocity at the structural grid points along the reed, both calculated at time step  $n$ . The fluid velocity along the reed is evaluated by the smoothed delta function,

$$\mathbf{U}^n = \sum_x \mathbf{u}^n(\mathbf{x}) \delta_h(\mathbf{x} - \mathbf{X}^n) \Delta x \Delta y \quad (\text{III.2.12})$$

where  $\Delta x$  and  $\Delta y$  are the grid sizes around the beam in  $x$  and  $y$  directions, respectively.  $\delta_h$  is chosen to be a four-point smoothed delta function (Peskin, 2002),

$$\delta_h(\mathbf{x}) = \frac{1}{\Delta x \Delta y} \varphi\left(\frac{x}{\Delta x}\right) \varphi\left(\frac{y}{\Delta y}\right) \quad (\text{III.2.13})$$

with

$$\varphi(r) = \begin{cases} 1/8 (3 - 2|r| + \sqrt{1 + 4|r| - 4r^2}) & 0 \leq |r| < 1 \\ 1/8 (5 - 2|r| + \sqrt{-7 + 12|r| - 4r^2}) & 1 \leq |r| < 2 \\ 0 & 2 \leq |r| \end{cases} \quad (\text{III.2.14})$$

The other variables are transferred between Eulerian and Lagrangian descriptions similarly. The method has been tested and validated for several benchmark problems involving fluid-structure interaction as well as forced convection with stationary and moving boundaries.

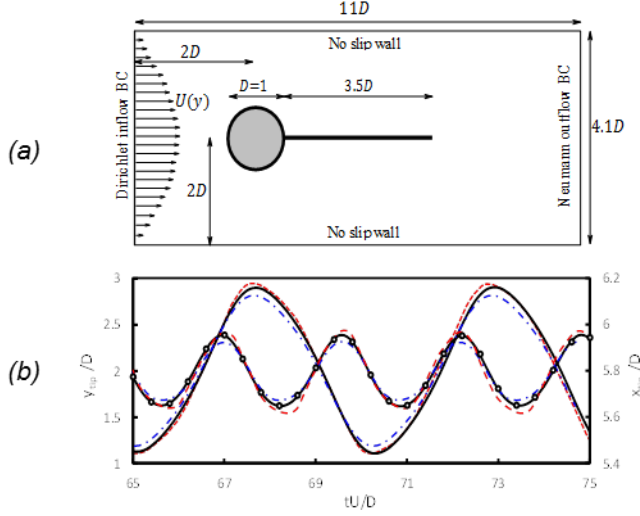


**Figure III.2-1.** (a) Schematic of the problem of flow-induced vibration of a flexible beam attached to a rigid cylinder. a) Stationary-state time histories of  $X$  and  $Y$  displacement of the tip of the beam. Red (dashed) lines is form Bhardwaj & Mittal, 2012; blue (dashed-dotted) line is form Turek and Hron, 2006 and black (solid line) is for the present method.  $\rho_s/\rho = 10$  and  $Re = \rho \bar{U}D/\mu = 100$ .

Cases	Sources	$A_m/D$	$St$	$C_D$
$\rho_s/\rho = 10$ , $Re = 100$	Present result	0.89	0.19	4.19
	Turek and Hron <sup>58</sup>	0.83	0.19	4.13
	Bhardwaj & Mittal <sup>63</sup>	0.92	0.19	3.56
	Tian et al. <sup>64</sup>	0.78	0.19	4.11
$\rho_s/\rho = 1$ , $Re = 200$	Present result	0.44	0.27	2.48
	Turek and Hron <sup>58</sup>	0.36	0.26	2.30
	Bhardwaj & Mittal <sup>63</sup>	0.41	0.28	2.20
	Tian et al. <sup>64</sup>	0.32	0.29	2.16

**Table III.2-1.** Amplitude of  $y$  motion at the tip of the beam ( $A_m$ ), the Strouhal number ( $St$ ), and the drag coefficient ( $C_D$ ) for the flow induced vibration of the beam behind a fixed cylinder.

We validate the fluid structure coupling model with flow-induced vibration of a flexible beam behind a fixed cylinder in a confined channel, originally proposed by Turek and Hron, 2006 as benchmark validation (Figure III.2-1, and Table III.2-1). The beam is inextensible with bending stiffness  $k_b = 0.933\rho D^3 \bar{U}^2$  which is equivalent to assuming Young modulus  $E = 1.4 \cdot 10^{-3} \rho \bar{U}^2$  for a beam with thickness  $h = 0.2D$  originally used by Turek and Hron<sup>58</sup>. In the current test, we consider two cases with 1)  $\rho_s/\rho = 10$  and  $Re = \rho \bar{U}D/\mu = 100$  and 2)  $\rho_s/\rho = 1$  and  $Re = \rho \bar{U}D/\mu = 200$ . Overall, our predictions agree very well with others, qualitatively and quantitatively, thereby providing confidence in the fidelity of the solver.

### III.2.2 2-D Modeling – Reed Dynamics

The reed is assumed to be fixed at the leading-edge and free at the trailing edge. A Lagrangian coordinate is chosen to be the arc-length along the reed starting at the leading-edge and ending at the trailing edge. The reed is modeled as a two dimensional body with zero-thickness and assumed to be elastic and inextensible with its dynamics governed by,

$$m_s \frac{\partial^2 \mathbf{X}}{\partial t^2} = \frac{\partial}{\partial s} (\sigma \mathbf{t} + q \mathbf{n}) - \mathbf{F} + \mathbf{F}_c \quad (\text{III.2.15})$$

where  $s$  is a Lagrangian coordinate along the reed,  $\mathbf{X} = [x, y]$  describes the material position of the reed,  $\mathbf{t} = \frac{\partial \mathbf{X}}{\partial s}$  is the unit tangent vector along the coordinate  $s$ , and  $\mathbf{n}$  is the unit normal vector. Furthermore,  $m_s$  is the excess mass per unit length of the reed. On the right-hand side of the equation,  $\sigma$  is the tension and  $q$  is the transverse stress. Finally  $\mathbf{F}$  is the force density applied by the reed on the surrounding fluid and  $\mathbf{F}_c$  denotes the force on the reed due to contact with the channel walls. The inextensibility constraint of the reed is expressed as  $\frac{d}{dt} \left| \frac{\partial \mathbf{X}}{\partial s} \right| = 0$  (Tornberg and Shelley, 2004, Huang, 2007), which is reformulated as an equation for the tension

$\sigma$  as,

$$\frac{\partial^2}{\partial s^2}(\sigma \mathbf{t}) \cdot \mathbf{t} = \frac{m_s}{2} \frac{\partial^2}{\partial t^2}(\mathbf{t} \cdot \mathbf{t}) - m_s \frac{\partial \mathbf{t}}{\partial t} \cdot \frac{\partial \mathbf{t}}{\partial t} - \frac{\partial}{\partial s} \left( \frac{\partial(q\mathbf{n})}{\partial s} - \mathbf{F} + \mathbf{F}_c \right) \quad (\text{III.2.16})$$

Using the Euler-Bernoulli assumption (Audoly and Pomeau, 2010) for a slender inextensible reed ( $M = k_b \kappa$ , with  $M$  the elastic moment along reed,  $k_b$  the bending rigidity, and  $\kappa = -\mathbf{n} \cdot \frac{\partial^2 \mathbf{X}}{\partial s^2}$  the local curvature along the reed), the transverse stress  $q$  becomes,

$$q = \frac{\partial M}{\partial s} = -\frac{\partial}{\partial s} \left( k_b \frac{\partial^2 \mathbf{X}}{\partial s^2} \right) \cdot \mathbf{n} \quad (\text{III.2.17})$$

To account for the support mechanism at the leading edge, we have also assumed that the reed is fixed at its first 6% of its length; and the free boundary condition at the trailing edge is enforced by imposing  $\partial^2 \mathbf{X} / \partial s^2 = 0$  and  $\partial^3 \mathbf{X} / \partial s^3 = 0$ .

We use the following nondimensional parameters to represent the inertia and bending rigidity of the reed,

$$M^* = \frac{\rho L}{m_s}, \quad U^* = UL \sqrt{\frac{m_s}{k_b}} \quad (\text{III.2.18})$$

where  $\rho$  is the density of the fluid. Physically,  $M^*$  represents the relative importance of the structural inertial force and  $U^*$  can be thought of as the ratio between the time scale related to the reed's natural oscillation in vacuum and the convective time scale of the fluid passing the reed.

Staggered grids are used on the reed along  $s$ ; the reed tension is defined on the centroid of the grid ( $i$ ) nodes and other variables are defined on the node vertices ( $i$ ). Equations (III.2.15) and (III.2.16) are then solved in the following sequence:

$$\mathbf{X}^* = 2\mathbf{X}^n - \mathbf{X}^{n-1} \quad (\text{III.2.19})$$

$$\begin{aligned} D(D(\sigma_i \mathbf{t}^*)) \cdot \mathbf{t}_i^* &= \frac{m_s}{2} \frac{1 - 2(\mathbf{t} \cdot \mathbf{t})_i^n + (\mathbf{t} \cdot \mathbf{t})_i^{n-1}}{\Delta t^2} - m_s (D\mathbf{V} \cdot D\mathbf{V})_i^n \\ &\quad - D(D(q\mathbf{n})^* - \mathbf{F}^n + \mathbf{F}_c^*) \cdot \mathbf{t}_i^* \end{aligned} \quad (\text{III.2.20})$$

$$m_s \frac{\mathbf{X}_i^{n+1} - \mathbf{X}_i^*}{\Delta t^2} - [D(\sigma_i D\mathbf{X}_i^{n+1}) + (q\mathbf{n})^{n+1}]_i = -\mathbf{F}^n + \mathbf{F}_c^* \quad (\text{III.2.21})$$

where  $\mathbf{X}^*$  is the predicted position of the reed at time  $n + 1$  and is used for calculation of all other intermediate variables with superscripts '\*'. The tension  $\sigma_i$  is calculated at the intermediate step and is used to update the position of the reed,  $\mathbf{X}^{n+1}$ . At the channel walls, we assume  $T = T_w$  with  $\Delta T_w = T_w - T_0$  denoting the increase with respect to the temperature of the incoming flow. The Neumann boundary condition is applied at the outflow boundary at  $x = 15L$ .

### III.2.3 Low-Order Models for Rapid Estimation

The current method employs a more physically realistic representation of the plate wake within the context of an inviscid flow (Figure III.2-2), and provides a theoretical prediction of the stability boundaries and vibrational characteristics of a plate confined in a channel. In particular,

a novel Green's function for the vortex sheet of the plate wake inside the channel as well as its rapidly convergent series approximation are proposed.

We focus on a two-dimensional problem in which a thin, flexible plate of length  $L$ , mass per unit length  $m_s$  and bending rigidity  $k_b$  is clamped at its leading edge and placed at a distance  $\eta$  from the lower wall of a channel with height  $H$ . The equations are non-dimensionalized using the fluid density  $\rho$ , incoming flow velocity  $U_0$  and  $L$ , resulting in four characteristic non-dimensional

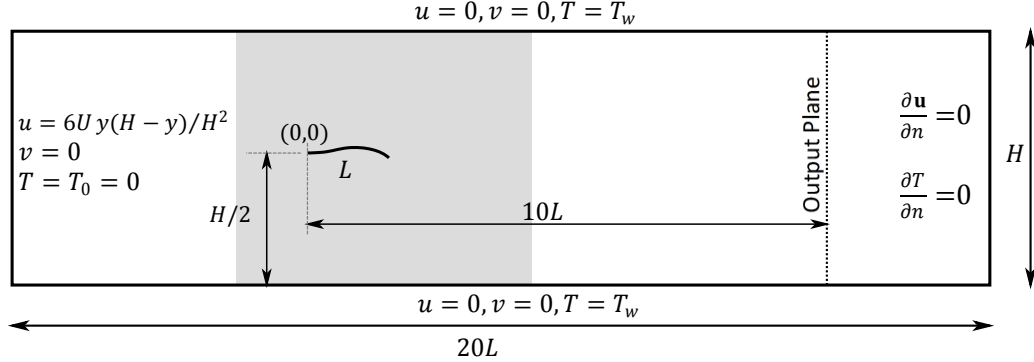


**Figure III.2-2.** The computational domain and assumed boundary conditions (not to scale).

parameters:  $M^* = \rho L / m_s$  (the mass ratio);  $U^* = U_0 L \sqrt{m_s / k_b}$  (the reduced velocity);  $h = H / L$  (the channel confinement ratio); and  $d = \eta / H$  (the plate placement ratio). The flow is assumed to be potential; the span of the plate is infinite; and the effect of viscosity is confined to the thin two-dimensional dipole bound vortex sheet along the plate and the deformable free vortex sheet associated with the wake of the plate.

To study the stability of the system, we assume a time-periodic solution for the vertical displacement and pressure jump and decompose them into their normal modes represented by  $Y$  and  $[P]$  respectively. Thus for example, the vertical position of the plate is defined as  $\xi = \text{Re}[Y(x)e^{i\omega t}]$ , where  $\omega$  is the complex eigen-frequency of the non-dimensional system of equations. In this description,  $\text{Re}(\omega)$  is the angular frequency and  $-\text{Im}(\omega)$  the growth rate of the normal mode. An unstable mode corresponds to  $\text{Im}(\omega) < 0$  and vice-versa. The resultant governing system of equations is:

$$\begin{aligned}
 -\omega^2 Y &= -\frac{1}{U^{*2}} \partial_x^4 Y - M^* [P], \\
 (i\omega + \partial_x) Y &= \frac{1}{2\pi} \int_0^1 \Gamma(x') G(x, x') dx' + W(x, \omega; \infty), \\
 \partial_x P &= (i\omega + \partial_x) \Gamma, \text{ with } P(1) = 0, \\
 Y(x=1) &= 0, \text{ with } \Gamma(x) = \frac{Y(x)}{\sqrt{x(1-x)}},
 \end{aligned} \tag{III.2.22}$$

where  $G(x, x')$  for a vortex sheet between two walls can be computed by the “method of images” by adding an infinite image system in the channel height direction (Greengard, 1990). The image system consists of vortex sheets of the same strength placed at  $(x, dh + 2jh)$  and vortex sheets with opposite strength placed at  $(x, -dh + 2jh)$  with  $j = (-\infty, \dots, \infty)$ .  $G(x, x')$



can be expressed as,

$$G(x, x') = \frac{\alpha}{2} \coth\left(\frac{\alpha}{2} r\right) - \frac{\frac{\alpha}{2} \sinh(\alpha r)}{\cosh(\alpha r) - \cos(2\pi d)}, \quad (\text{III.2.23})$$

$$\text{with } r = x - x', \quad \text{and} \quad \alpha = \frac{\pi}{h} \dots$$

The effect of the free vortex sheet  $W(x, \omega; \infty)$  takes a much simpler form due to the conservation properties of circulation in the free vortex wake. In addition, the total circulation in the plate is also periodic,  $\lambda(x = 1, t) = \text{Re}(\Lambda_0 e^{i\omega t})$  where  $\Lambda_0$  is the amplitude of  $\lambda$  at  $x = 1$ . Given that any fluid particle at  $(x, t)$  was located at the trailing edge ( $x = 1$ ) at time  $t - (x - 1)$ , its circulation can be expressed as  $\lambda(x, t) = \Lambda_0 e^{i\omega(t-(x-1))}$  and consequently we have,

$$W(x, \omega; \infty) = -\frac{\omega \Lambda_0}{2\pi} \int_1^\infty e^{-i\omega(x'-1)} G(x, x') dx' \quad (\text{III.2.24})$$

The presentation of the confined plate results begins by showing in Figure III.2-3, a comparison between the current prediction of the stability boundary of the plate placed in the middle of a channel with  $H/L = 1$ , with the fully nonlinear fluid-structure interaction simulations by, and the previous analytical method by Guo and Paidoussis, 2000 with the upstream wake assumption, and the stability boundary predicted by Alben, 2015 with the regularized large deflection vortex method. For the fully viscous simulation, we selected  $Re = 400$  and a series of 250 Navier-Stokes simulations were carried out to cover a range of  $M^*$  from 0.03 to 30 and  $U^*$  from 3 to 16. Each simulation was integrated in time till about  $t = 100L/U$  in order to eliminate transient effects and obtain representative asymptotic deflection amplitudes. The stability boundary from the current method shows a good agreement with the Navier-Stokes simulations both for the lower range as well as the higher range of  $M^*$  values.

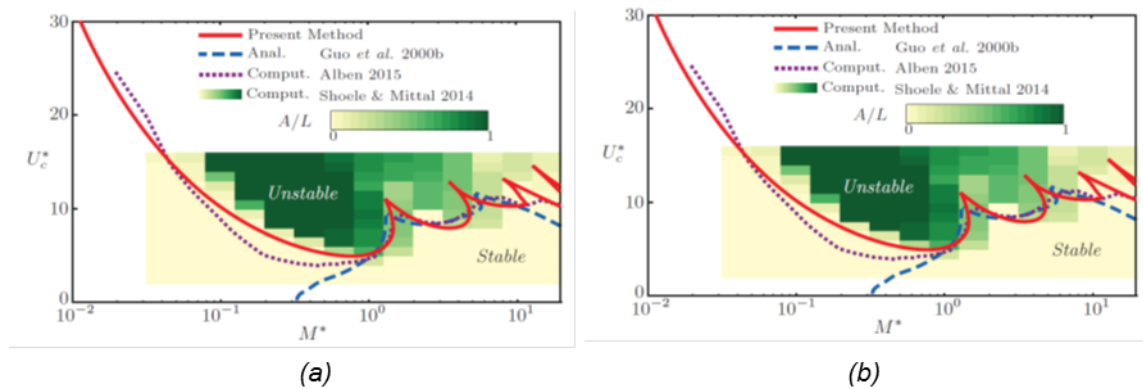


**Figure III.2-3.** (a) Comparison of the stability curves of the confined plate with the confinement ratios  $H/L = 1$  and  $\eta/H = 0.5$  between present method (solid line), analytical prediction by Guo and paidoussis, 2000 with the upstream wake assumption (dashed line), numerical prediction using large deflection vortex method by Alben et al., 2015 and the fully nonlinear fluid-structure interaction simulations at  $Re = 400$  from Shoele & Mittal, 2014(contour plot).  $A$  is the peak-to-peak amplitude of the motion at the trailing edge of the plate. Right) Stability curves for the confined plate for different confinement ratios  $H/L$ . The data in this plot is for  $\eta/H = 0.5$

In Figure III.2-3 we compare the stability boundaries of the plate for different confinements ranging from  $H/L = 10$  down to  $1/10$ . The cases with  $H/L > 0.5$  have very similar stability curves, with the main differences appearing at small  $M^*$  values. When  $M^*$  reduces below 1,  $U^*$  first reduces rapidly and then increases with further decrease in  $M^*$ . Furthermore, the onset of this increase in  $U^*$  happens at smaller  $M^*$  values for increased confinements. For heavier plates (smaller  $M^*$ ), the confinement effects by the channel walls reduce the critical velocity  $U^*$ , indicating that for a similar inflow speed and plate mass ratio, confinement increases the instability of heavy reed. Similar behavior has been found in our previous viscous flow simulations.

### III.2.4 Heat Transfer Performance with Reeds

The amplitude of the reed oscillation is denoted by  $A/L$  and the reed vibration Strouhal number with  $St_A = f_A L/U$  in which  $f_A$  denotes the dominant oscillating frequency of the reed. Unless otherwise noted, all output flux are calculated at a cross section  $X_o = 10L$  downstream of the leading-edge of the reed. In particular, the net change in the thermal energy of the fluid is,

$$Q = \int_0^H \rho C_p u (T - T_0) dy \quad (III.2.25)$$

where the integration is performed at  $x = X_o$  As indicated in Figure III.2-2. The time-averaged value of the  $Q$  is indicated with  $\bar{Q}$ , the magnitude of its temporal variation with  $\Delta Q = \text{s.d.}(Q)$  (the standard deviation of  $Q$ ), and a thermal Strouhal number with  $St_Q = f_Q L/U$  where  $f_Q$  is the dominant frequency of heat flux at  $x = X_o$ . In addition, the net energy loss due to pressure drop between the inflow and output plane is calculated as,

$$\dot{E} = \int_0^H (p - p_\infty) u dy \Big|_{x=0} - \int_0^H (p - p_\infty) u dy \Big|_{x_o} \quad (III.2.26)$$

The thermal enhancement factor ( $TEF$ ), defined as the ratio of the mean heat transfer through the output plane of a channel with the reed  $\bar{Q}$  to the mean heat transfer through the output plane of a channel without the reed  $\bar{Q}_0$  at an identical pumping power (Gee and Web, 1980, Tsia and Hwang, 1998, Ozceyhan et al., 2008, Promvongse et al., 2010), is used to compare the performance of the reed enhanced channel to a baseline channel with no reed. This TEF is given by:

$$TEF = \frac{\bar{Q}}{\bar{Q}_0} \times \left( \frac{\bar{E}_0}{\bar{E}} \right)^{1/3} \quad (III.2.27)$$

where  $\bar{E}_0$  is the mean energy loss between the inflow and output plane in the channel without a reed and a  $TEF$  value greater than 1 indicates higher heat transfer for the same input mechanical power. In addition, the convective heat transfer on the channel walls are quantified via the Nusselt number ( $Nu$ ) defined as,

$$Nu = \frac{\partial(T_w - T)/\partial n|_s}{\Delta T_w/L} \quad (III.2.28)$$

with  $n$  being the normal direction to the walls pointing into the fluid region.

Figure III.2-4 shows the mean heat flux per unit length of the height of the channel at the output plane ( $\bar{Q}$ ) and the thermal enhancement factor ( $TEF$ ). In the stable cases where the reed remains

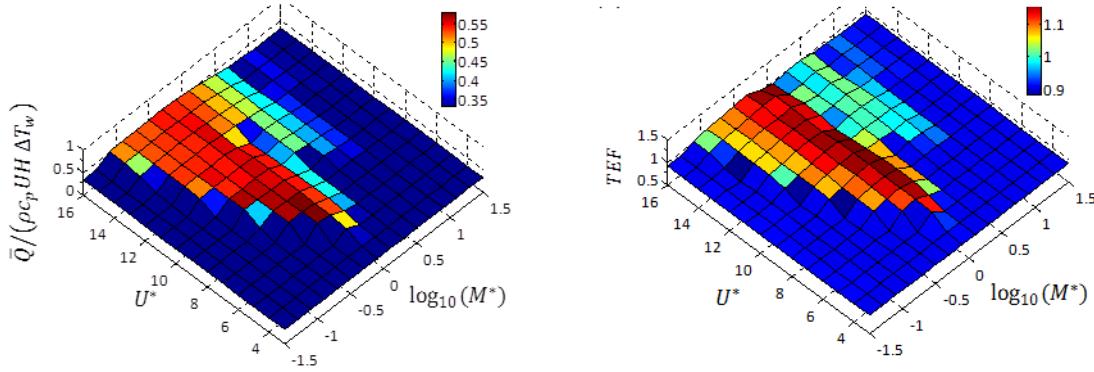


**Figure III.2-4.** Effect of  $M^*$  and  $U^*$  on the non-dimensional mean heat flux per unit height and thermal enhancement factor. All coefficient are calculated at  $10L$  downstream of the reed leading edge.

fixed, the presence of the reed only has a negligible effect on the heat flux (with  $\bar{Q}/(\rho c_p UH \Delta T_w) = 0.33$  compared to 0.32 in the channel without the reed). However, in the finite range of  $\log_{10} M^*$  and  $U^*$  (almost coincident with high amplitude region in Figure III.2-4, the channel with the flexible reed shows much higher heat flux at the output plane with the maximum  $\bar{Q}/(\rho c_p UH \Delta T_w) = 0.56$  occurring at  $[\log_{10} M^*, U^*] \sim [-0.3, 8]$ .

For the case with  $M^* = 1$  and  $U^* = 4$  the reed stays stationary and the flow exhibits features of a steady wake (Figure III.2-5i). For  $U^* = 8$  and 12, the reed oscillates with a large amplitude and the amplitude of motion in this case grows rapidly from the leading edge to the trailing edge. These cases generate a well-organized vortex street where vortices of opposite rotation entrain hot fluid away from the wall. In both these cases, the counterclockwise (CCW) vortices are concentrated mostly near the top wall and the clockwise (CW) close to the bottom wall. As the reed becomes more flexible ( $U^* = 16$ ), it vibrates in a new mode shape and the reed deflection for this new mode shape occurs predominantly near the trailing edge (Figure III.2-5 (ii)) with a clear transition in the vortex structures that causes larger energy deficit and lowers the TEF in this case.

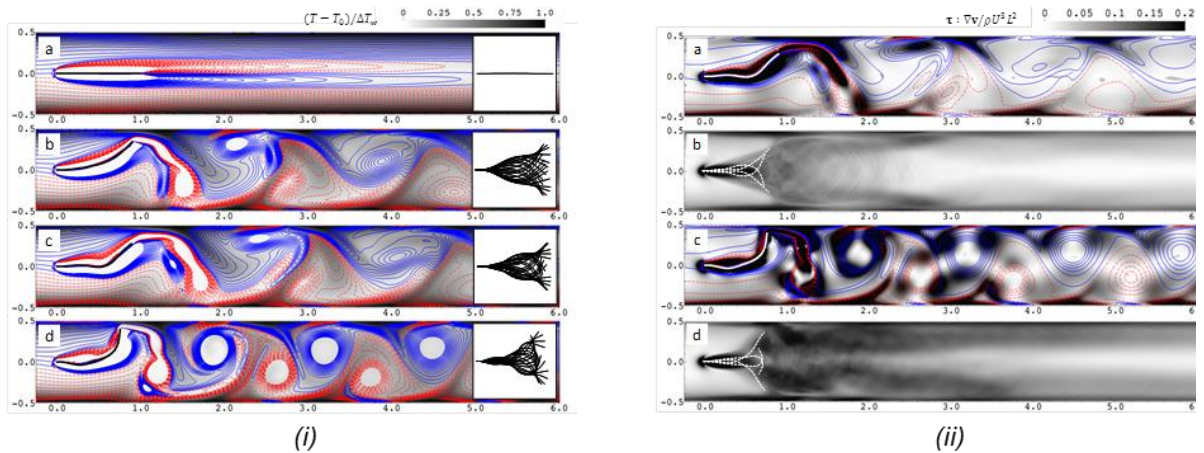


**Figure III.2-5.** (i) Vorticity (line) and temperature contours (colored) of a reed with  $M^* = 1$  and a)  $U^* = 4$ , b)  $U^* = 8$ , c)  $U^* = 12$ , and d)  $U^* = 16$ . (ii) Instantaneous (a and c) and mean (b and d) viscous dissipation ( $\tau : \nabla v$ ) inside the channel with the reed with  $M^* = 1$  and ((a) and (b))  $U^* = 12$ , ((c) and (d))  $U^* = 16$ .

This effect becomes more apparent by examining the distribution of the viscous dissipation inside the channel. In figure III.2-5 (ii), Comparison of the contours of instantaneous viscous dissipation in Figure III.2-5 right a and c, shows that while in the case of  $U^* = 12$  the regions with high dissipation coincides with the locations of large heat flux, in the case of  $U^* = 16$  there is significant increase in the area of large  $\tau : \nabla \mathbf{v}$  in the middle of the channel. Comparison of the mean viscous dissipation for these cases indicates that there is a large increase in  $\tau : \nabla \mathbf{v}$  (dark contour color in Figure III.2-5 right c and d) in both the near wake of the reed, and far downstream for  $U^* = 16$  compared to  $U^* = 12$ .

In figure III.2-6, we plot  $\bar{Q}$  and  $TEF$  as a function of  $Re$ . In all three cases with the reed as well as the case without the reed,  $\bar{Q}$  reduces monotonically with increasing  $Re$ . This decrease is attributed to the reduction in the rate of heat diffusion at the walls with increasing  $Re$ , which reduces the effective heat flux from the walls. Figure III.2-6 shows the variation of  $TEF$  for these cases and this plot shows a rapid initial increase in  $TEF$  for all cases. The rate of this increase however decreases at larger  $Re$  values with the  $TEF$  approaching an asymptotic value. More flexible reeds (higher  $U^*$ ) reach their maximum  $TEF$  values at the smaller  $Re$  numbers. The  $U^* = 14$  has the lowest  $TEF$  among all the cases, while the  $TEF$  for  $U^* = 8$  and  $U^* = 12$  shows a very similar trend with  $Re$  up to  $Re = 600$ . The maximum gain in thermal performance as quantified by  $TEF$  reach up to about 25% for the cases studied here and these occur at the higher Reynolds numbers.

At  $Re = 50$ , the changes in the flow due to the reed oscillation dissipate rapidly and the flow returns back to the baseline channel flow. Since diffusion plays an important role in this case, the

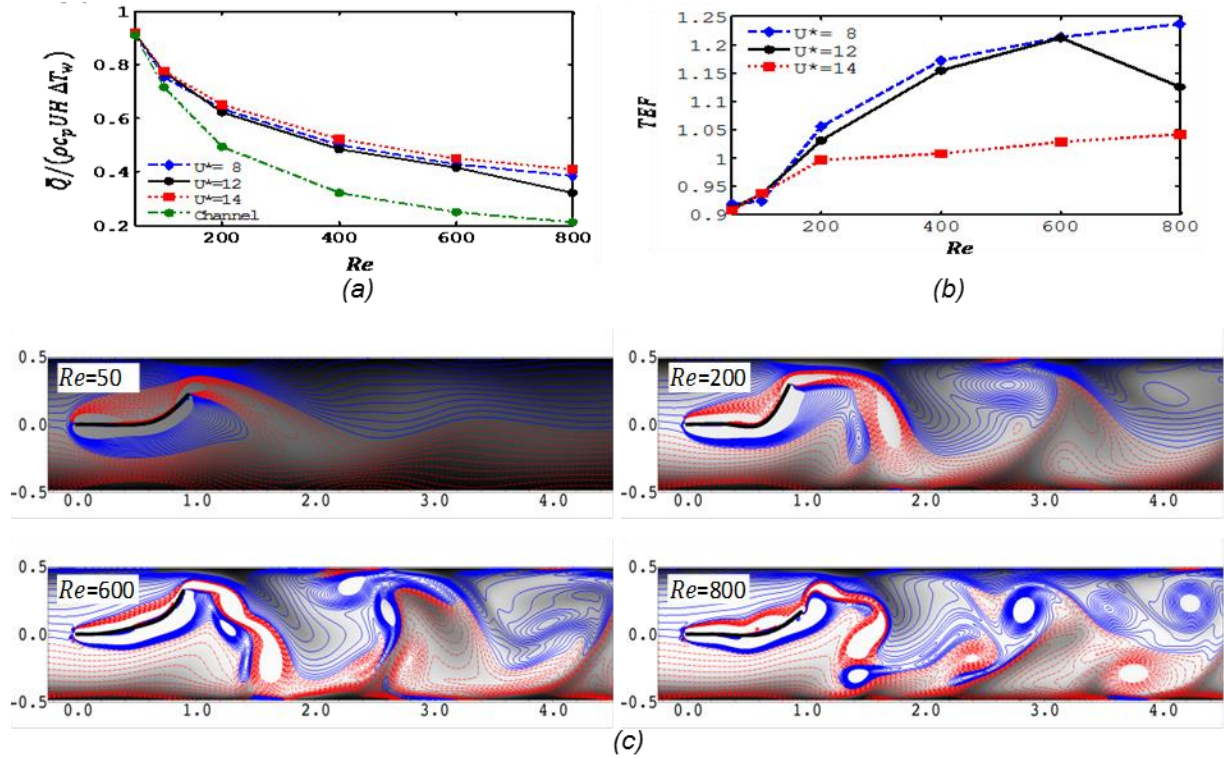


**Figure III.2-6.** (a) and (b) Dependence of  $\bar{Q}$  and  $TEF$  on the value of  $Re$  for a reed with  $M^* = 1$ . The green lines are for a channel without the reed. (c) Vorticity (line) and temperature contours (colored) of a reed at different  $Re$  for a reed with  $M^* = 1$  and  $U^* = 12$ .





The heat enhancement capacity is related to the main characteristics of the flow and temperature field in Figure III.2-7a in which the snapshots of three dimensional vorticity iso-surfaces are shown and are correlated to the isothermal contours in three perpendicular cross section marked in the channel. The temperature distribution of the sections is shown with the color contours while the corresponding vorticity contours shown with thick lines. In addition, the sequence of the reed deformation and the comparison of two-dimensional simulations and the corresponding three-dimensional simulations are shown in Figure III.2-7b.

### III.2-6 Investigation of Reed Shape

Analysis of heat transfer enhancement due to a fluttering reed in a heated channel using Navier-Stokes multiphysics simulations was performed for a number of reed shapes and channel configurations. Figure III.2-8 shows the schematic of a typical simulation with constant temperature top and bottom walls, and adiabatic front and back walls.

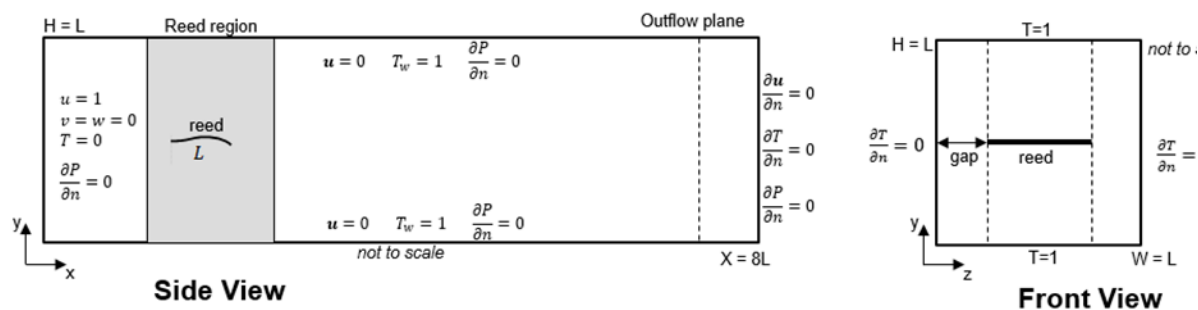


**Figure III.2-8.** Schematic of typical 3D Navier-Stokes multiphysics simulation. Uniform inflow at the inlet at  $temp=0$ . Top and bottom walls at  $temp=1$ , front and back walls are adiabatic.

This system has a large parameter space which is further complicated in 3D as reed shape and channel configuration bring in new parameters. To begin exploring this space, simulations were chosen to identify and investigate the dominant physics responsible for the observed heat transfer enhancement. The goals of these simulations were as follows. 1) Investigate the dominant heat transfer enhancement mechanism and associated flow structures. 2) Identify reed shape and channel configuration parameters responsible for said beneficial flow structures. 3) Assess key parameters towards shape optimization and examine sensitivity to those parameters. Fully implicit FSI coupling of the reed motion and the flow is numerically expensive. In 3D these issues are compounded, making a large number of 3D FSI simulations practically difficult. To accelerate the experimental process and facilitate broader exploration, a prescribed motion

method was developed to decouple the reed motion from the fluid simulation. Using the results of our prior 2D FSI parametric sweep, the best performing case (by *TEF*) was chosen. The reed motion data was then extracted, modeled as a traveling wave, and applied to the entire span of the 3D reed.

A number of interesting phenomena and trends have been observed. As an example, the focus here will be on one particular phenomenon observed when comparing the rectangular reed with the notched reed. The notch reed was selected to examine the effect of spanwise vorticity production on heat transfer enhancement as the notched reed will produce less spanwise vorticity at the trailing edge. Figure III.2-9 shows a performance comparison between the rectangular and notched reed cases. The decrease in heat transfer suggests that spanwise vorticity production may play a role in heat transfer enhancement. However the decrease in energy loss shows a link

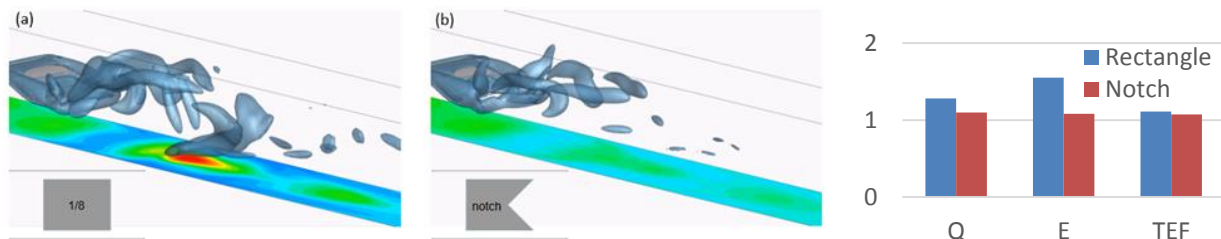


**Figure III.2-9.** A 3D snapshot view of the (a) rectangular reed and (b) notched reed. The blue iso-surfaces are vortical structures and the color on the bottom wall is the heat transfer. (c) Comparison of heat transfer ( $Q$ ), energy loss ( $E$ ), and thermal enhancement factor ( $TEF$ ) for rectangular vs. notched reed

between heat transfer enhancement and energy loss. To further examine these effects to see if they can be decoupled, shows a 3D view of the flow structures and heat transfer comparing these cases at a single time step.

Here we can see a few key differences which speak to the core of the heat transfer enhancement mechanism. Qualitative comparison of the heat transfer through the bottom wall shows a significant spike for the rectangular case which is absent from the notched case. This “hot spot” is responsible for the increased heat transfer for the rectangular case observed in Figures III.2-9a and b. Above this hot spot is a vortical structure which is absent from the notched case.

Qualitative observation of the flow structures for all simulations showed a strong correlation between the presence of this particular flow structure and areas of high heat transfer at the wall. This result suggests that this structure may be responsible for the heat transfer enhancement due to the reed. While this reed shape analysis shows that there are further benefits to be found with respect to heat transfer enhancement, the examples tested in the present study already provide significant heat transfer enhancement. Further research could examine the genesis and evolution of this vortical structure as it is convected downstream, its involvement with heat transfer at the wall, and its role in energy loss due to the flapping reed. The goal would be to develop a reed shape that can produce heat transfer enhancing structures without as much energy loss, leading to further improvements in TEF.

### III.3 Experimental Investigations

The experimental investigations focused on mechanisms for improving the heat transfer characteristics within a high aspect ratio channel at transitional Reynolds numbers that is typical of air-side heat exchangers. Heat transfer is enhanced by the deliberate formation of small-scale vortical motions that are effected by aeroelastically fluttering thin reeds cantilevered across the span of the channel. The reed's concave/convex surface undulations lead to the time-periodic formation, advection, and shedding of vorticity concentrations that scale with the motion amplitude and the channel width. The reed motion is captured using phase-locked imaging, and its interactions with the core flow and surface boundary layers are investigated using high-resolution PIV. Phase-averaged distributions of the reed's mechanical energy demonstrate variations of the vibration modes across the channel. The reed interactions with the surface are accompanied by transitory shedding of vorticity concentrations that interact with the surface vorticity layer and lead to a local increase in the flow's turbulent kinetic energy and to a strong increase in heat transfer. The streamwise evolution of the reciprocal interactions between the reed and the channel flow are captured using cross stream velocity distributions along the channel that link the kinetic energy shape factor to the rise in heat transfer (e.g.,  $Nu$ ) relative to the base flow. It is shown that the reed-induced heat transfer increases with  $Re$  and results in significant improvement in the global coefficient of performance

#### III.3.1 Experimental Setup and Diagnostics Procedures

The interactions of the reeds with the cross flow within a prototypical channel are investigated using a modular test bed comprising a metered, compressed air source followed by miniature internally-partitioned diffuser, a primary contraction (contraction ratio 25:1), and a tests section having a constant cross section measuring 25 x 25 mm, 254 mm long as shown in Figures III.3-1a and b. The present setup enables testing of higher aspect ratio channels that are connected to the primary contraction via a secondary contraction (fabricated using stereolithography) that sets the variable channel width (and aspect ratio). The higher aspect ratio channels (all 25 mm high) have side walls that are inserted within parallel grooves at the top and bottom walls of the primary (25 mm wide) channel and mate into the secondary contraction as shown schematically in Figure III.3-1c. The present experiments focus on 25 and 5 mm wide channels where the side walls of the 5 mm channel are either transparent (for PIV measurements) or include thin film

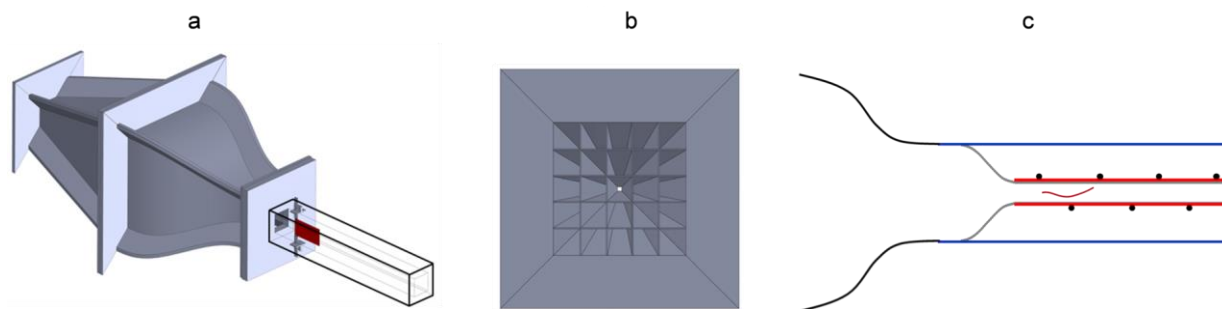


**Figure III.3-1.** CAD drawings of the 25 mm wide channel setup: a) The flow duct assembly including a diffuser, 2-D contraction, and the channel test section with a mounted cantilevered reed (red); b) Upstream view of the partitioned diffuser; and c) Top view of the flow path from the primary contraction to a high aspect ratio channel insert showing the secondary contraction and the side wall inserts of the 5 mm wide channel. The placement of the reed is also shown schematically along with the film heaters (in red) and streamwise locations of the thermocouple sensors (marked by •) for heat transfer measurements.



heaters for heat transfer measurements (Figure III.3-1c). The channel assembly is equipped with static pressure ports at the inlet and exit of the test section and at the exit of the primary contraction.

Interchangeable reeds are laser fabricated using an array of thin-film materials. In the present investigations, the reeds are primarily fabricated from polyester sheets of varying thickness having nominal Young modulus  $E = 5$  GPa and density  $\rho_{\text{reed}} = 1,300$  kg/m<sup>3</sup>. Each reed has a rectangular planform, and spans nearly the entire height of the channel (23 mm). The lengths of the present reeds are varied between 30 mm and 50 mm, and the thickness of the film material is varied between 13 and 50  $\mu\text{m}$ . The reed is cantilevered within the centerplane of the channel using a fixture that clamps it along its upstream edge between two stainless steel segments 0.1 and 0.025 mm thick to minimize blockage losses (Figure III.3-3). The cantilever fixture is mounted within the test section through two access holes within the opposite (top and bottom) walls. The tension of the cantilever assembly is adjusted using a torque wrench to ensure repeatability in the mounting.

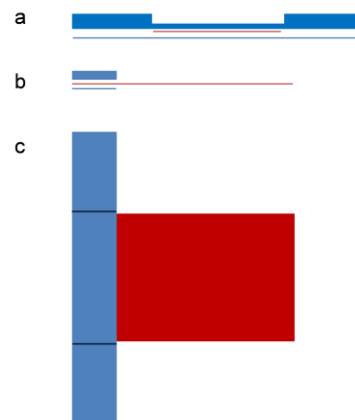


**Figure III.3-2.** Front (a), side (b) and top views of the cantilevered reed mounting fixture. The spanwise recess of the top clamp spans the height of the channel's test section to minimize blockage.

The reed motion is characterized by imaging a trace along its mid-span (between its upstream and downstream edges) that is illuminated using a pulsed YAG laser sheet normal to the channel's centerplane. The scattered light from the intersection of the laser sheet and the reed is imaged using a CCD camera that is mounted above the channel's test section such that its optical axis is within the channel's centerplane, and parallel to the reed's leading edge (the field of view is similar to the upstream field of the PIV setup shown in Figure III.3-3). The camera is synchronously triggered with the laser to provide an image of the centerline during a given instant in time during the reed's oscillation cycle when a set point along the surface of the reed is at a given cross stream position as measured using a laser position sensor (having a resolution of 36  $\mu\text{m}$ ). For imaging the reed's centerline, the position sensor is placed 5 mm upstream of the downstream tip of the reed (at rest), and its output is used to create a clear phase reference that triggers the YAG laser and CCD camera when the reed's tip is located at a number of predetermined (normally, equally-spaced) cross stream positions along the width of the channel



**Figure III.3-3.** The PIV field of view of the flow in the  $x$ - $y$  plane of the 25 mm wide channel  $z = H/2$  over the reed and downstream of its trailing edge. Multiple streamwise positions of the laser sheet are shown with some overlap. The laser beam of the range finder is also shown for reference within the reed's shadow (shown in gray).

(along the  $y$  coordinate) using a comparator. The images of the reed's centerline are digitized and since the reed's motion along its length varies somewhat from cycle to cycle as it oscillates across the channel, these images are conditionally-averaged to yield the *most probable*  $x$ - $y$  coordinates of the reed's centerline at each of the set cross stream positions. These data are used for the characterization of the reed's dynamics as discussed further in Section III.3.2.

The flow fields over the reed's surface and downstream of its trailing edge are measured using particle image velocimetry (PIV). A top view of the optical setup is shown in Figure III.3-3. Similar to the measurements of the position of the reed's centerline, the PIV images are acquired at each of multiple set positions of the same reference point on the reed's centerline (5mm upstream of its trailing edge) across the channel's width. The PIV YAG laser and CCD camera are triggered using the laser position sensor, as described above. Fog particles having an average diameter of 50  $\mu\text{m}$  are used for the PIV measurements. For each cross stream position of the reed, 170 image pairs are acquired, and the most probable velocity field is computed using a subset of the captured PIV images to produce a flow field that is locked to the motion of the reed. In addition, the time-averaged flow field across the width of the channel is acquired at multiple streamwise locations using 600 image pairs at each location.

Heat transfer measurements in the 5 mm channel are conducted using thin aluminum sidewall inserts that are integrated with uniform film heaters and are insulated from behind (using an air gap) as shown in figure III.3-1c. Each of the heated side walls are instrumented with seven equally-spaced T-Type thermocouple sensors (the air inlet temperature is measured separately). The temperature and velocity distributions at the exit plane of the channel are also measured using miniature 0.25 mm diameter T-type thermocouple sensor and 0.5 mm diameter pitot tube mounted on an external, high-resolution traversing mechanism, and is used to compute the heat transfer characteristics of the channel flow.

### III.3.2 Characterization of Reed Dynamics

The velocity of the embedding flow at which the onset of reed motion occurs within the channel (the critical speed), and the magnitude of the dominant frequency of the ensuing oscillation past this speed depend upon the reed's geometry (length and thickness), its density, and the density of the embedding fluid (Shelley et al., 2005). The present investigations have demonstrated that the presence and proximity of the channel walls can also affect the critical speed and the oscillation frequency (cf. §III.2). The onset of the reed oscillation is demonstrated in Figure III.3-4. In order to characterize the onset of oscillations, for a reed of given geometry ( $L = 45$  mm,  $t = 38$   $\mu\text{m}$ ,  $w = 23$ mm) and mechanical properties, the air speed in the channel was increased gradually (at a rate of about 16 cm/sec/sec) using a flow controller that is built into the air supply (cf., §III.3.1) while monitoring the motion of a given point on the reed's surface (at center span, 5 mm upstream of its trailing edge) using the laser proximity sensor (cf., Figure III.3-4). Figure III.3-4 shows the temporal variation of the oscillation amplitude at the tip of the reed as the channel speed is increased between 4.72 and 4.88 m/sec at a rate of about 16 cm/sec/sec. When the flow speed is below the onset of oscillations, the reed exhibits a mild flutter with a nominal amplitude  $A_{\text{reed}}/w < 0.05$  (note that the tip of the reed is normally slightly offset relative to the center of the channel (less than  $0.01w$ ). As the air speed increases, the amplitude of the oscillation begins to increase noticeably for  $t > 500$  msec, and the critical speed when the oscillation amplitude exceeds  $0.05w$  is  $U_{\text{crit}} = 4.8$  m/sec (the oscillation period is approximately  $T = 27$  msec or  $St_L = 0.34$ ). The oscillation amplitude reaches a quasi-steady magnitude  $0.26H$  within 6 oscillation cycles. The oscillation frequency increases to 45 Hz as the speed increases to  $U = 4.88$  m/sec).

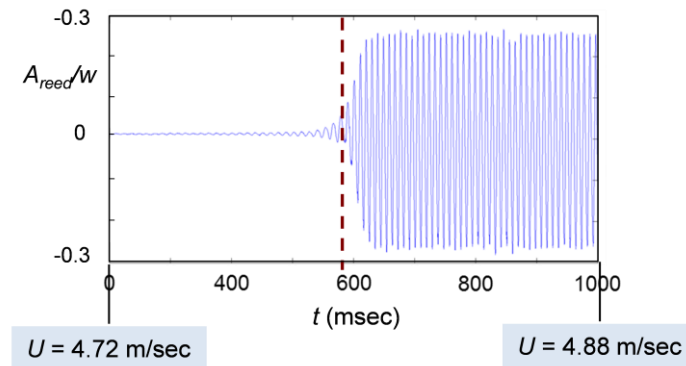


**Figure III.3-4.** The variation with time of the oscillation amplitude at the tip of the reed (thickness and length are 38 mm and 45 mm, respectively). The time traces of the tip's motion shows the onset of oscillations as the channel speed is gradually increased between 4.72 and 4.88 m/sec through the reed's critical velocity (defined as the speed at which  $A_{reed}/W = 0.05$ ). The initial reed tip offset (at  $t = 0$ ) relative to the center of the channel is less than 1% of the channel width.

The critical velocity was measured for several reed thicknesses and lengths  $t = 13, 25$ , and  $38$ , and  $50 \mu\text{m}$  and  $L = 30$  and  $45 \text{ mm}$  using the procedure described in connection with Figure III.3-5. Following the procedure of Shelley et al. (2005), Figure III.3-5 shows the variation of the reduced critical velocity with the reed's inertia ratio. The reduced critical velocity  $U^* = U_{crit}(\rho_{air}L^3/k_b)^{0.5}$  ( $k_b$  is bending stiffness per unit span) is a measure of the ratio of kinetic energy of the air flow to the reed elastic potential energy, while reed's inertia ratio  $S$  is the ratio of the mass (per unit area) of the reed to the mass of the air with which it interacts  $S = \rho_{reed}t/\rho_{air}L$ . In these experiments, independent measurements of the critical speed were repeated four times for each of four samples of each reed configuration, and the variance of each set of 16 measurements is shown in a gray band around the data symbols. The inviscid 2-D model of a free reed of Shelley et al. (2005) is also shown for reference. These data show that the reduced critical velocity decreases nearly exponentially with increasing inertia ratio (as the reed becomes heavier compared to air), and appears to asymptote to  $U^* \approx 12$  for  $S > 1.5$  (or essentially a constant critical Reynolds number for a given channel width and reed length). It is remarkable that the

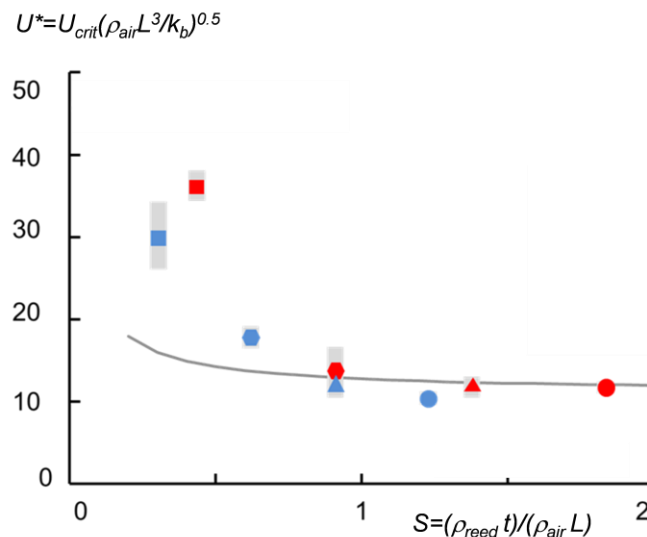


**Figure III.3-5.** Variation of the (dimensionless) critical flow speed ( $U^*$ ) with the inertia ratio of the reeds ( $S$ ) for several reed thicknesses (and lengths):  $t = 13 \text{ mm}$  [ $L = 30 \text{ mm}$  (■) and  $45 \text{ mm}$  (■)],  $25 \text{ mm}$  [ $L = 30 \text{ mm}$  (◆) and  $45 \text{ mm}$  (◆)],  $38 \text{ mm}$  [ $L = 30 \text{ mm}$  (●) and  $45 \text{ mm}$  (●)] and  $50 \text{ mm}$  [ $L = 30 \text{ mm}$  (▲) and  $45 \text{ mm}$  (▲)]. The grey bar corresponding to each data point represents the deviation. A comparison with the potential flow model (Shelley et al., 2005) is shown using a solid gray line.

measurements agree well with the model for  $S > 0.8$  indicating that the proximity of the channel walls, viscous effects, and 3-D modes of the reed motion become less important as the mass of the reed is increased. The increasing deviation between the model and the measured critical speed when  $S$  decreases indicates that these effects are more prominent, and it is reasonable to assume that probably 3-D modes of the thinner (lighter) reeds are the main contributors. The variation with  $S$  also indicates that for given density ratio and reed thickness, the deviation from the free reed increases as  $S$  decreases with increasing reed length as its interactions with the channel's side walls and the alternating constricted flow along each of the reed surfaces alter the distribution of side forces due to vortex shedding.

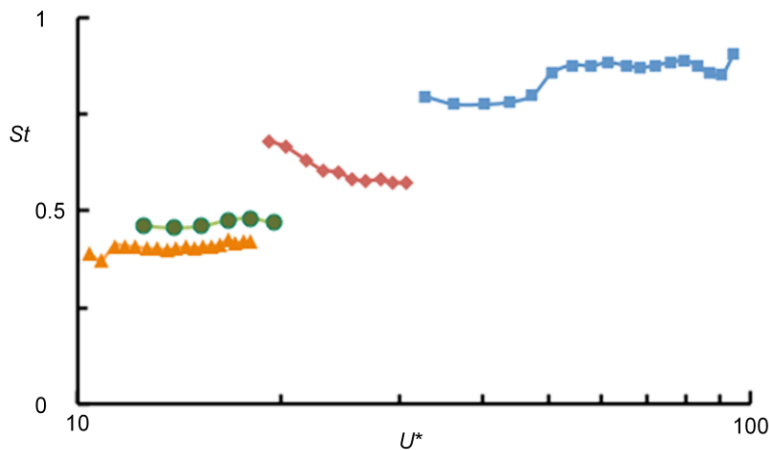


**Figure III.3-6.** Variation of the reed's Strouhal number  $St_L$  ( $L = 45$  mm) based on the spectral component at the fundamental frequency with the reduced channel velocity  $U^*$  for  $t = 13$  mm (■), 25 mm (◆), 38 mm (●), and 50 mm (▲).

The motion of the reed is also characterized in terms of its oscillation frequency that was assessed from time traces of the motion of the tip of the reed. Figure III.3-6 shows the variation of the fundamental oscillation frequency (computed using FFT of the time trace, and given by the Strouhal number) with the reduced velocity based on the channel's average velocity  $U^* = U_{ch}(\rho_{air}L^3/k_b)^{0.5}$ , where  $k_b = EI$  is the bending stiffness ( $E$  is Young's modulus of the reed, and  $I = t^3/12$  is the area moment of

inertia per unit width). As noted above,  $U^*$  is a measure of the ratio of kinetic energy of the air to the reed's elastic potential energy, and therefore while for a given reed geometry  $U^*$  increases linearly with  $U_{ch}$  (and with the Reynolds number), for a given channel velocity,  $U^*$  decreases with increasing reed thickness like  $t^{-1.5}$  yielding distinct ranges of  $U^*$  when the reed thickness  $t$  is increased incrementally from 13 to 50  $\mu\text{m}$  ( $L = 45$  mm). It is noted that for these data sets, the channel Reynolds number varies within the range  $1000 < Re < 10,000$ . It is remarkable that while for the thinner reeds  $St_L$  varies with the channel speed owing to the presence of 3-D modes as is also evident from the variance in the oscillation frequency at each speed, the oscillation frequency of the thicker reeds is nearly independent of the reduced velocity and therefore varies linearly with the channel speed.

The reed's oscillation past the critical velocity was analyzed using a trace along its centerline (through mid-span) at a given instant during the oscillation cycle that is imaged as described in §III.3.1. The conditionally-averaged traces of reeds in the 25 and 5 mm channels when their tips are located at 39 equally-spaced positions across the width of the channel are shown in Figures III.3-7a and b, respectively. These data are captured at an (average) channel speed of 5 m/sec for nearly-identical, 38  $\mu\text{m}$  thick reeds that are 45 and 50 mm long in the 25 and 5 mm channels, respectively so that they have the same nominal critical velocity. These data show that the motion of the reed is reasonably symmetric about the centerline of both the 25 mm and 5 mm

channels. However, while in the 25 mm channel the reed comes in contact with the side walls only near its tip, in the 5 mm channel the motion of the reed is strongly affected by interactions with the walls as the reed's surface attaches to each of the walls along up to  $0.06L$  upstream of its tip. Such contact clearly affects the evolution of the flow along the surface and may produce some suction force that leads to progressive upstream attachment. As discussed in connection with Figures III.3-12, the

attachment leads to a momentary increase the mass flow rate on the back side of the reed and lower pressure while the pressure on the closed side is building up due to blockage. It is this imbalance that contributes to the restoring force that leads to detachment from the surface and motion towards the opposite wall of the channel. Since the flow along the far side of the reed (relative to the attaching wall) is diffusing in the streamwise direction (owing to the streamwise increase in the open cross section), the static pressure along the surface decreases in the streamwise direction leading to a larger restoring force near the tip of the reed. It is noteworthy that this mechanism is not present in the absence of the walls (or when the reed is sufficiently removed from the walls) when the motion is primarily dominated by nominally time-periodic interaction with vortex shedding.

The effects of the interactions with the channel's sidewalls on the motion of the reed are also assessed using modal analysis based on proper orthogonal decomposition (POD) of the centerline traces in Figure III.3-8. The energy distribution of the reed's modes within the 25 and 5 mm channels (Figure III.3-8a) shows that Modes 1-3 capture over 90% of the modal energy in both channels (Mode 1 captures nearly 80% and 70% of the energy in the 25 and 5 mm channels, respectively). The lower energy associated with Mode 1 in the 5 mm channel is commensurate with the higher energy of Mode 2 compared top the 25 mm channel and is evidently the result of the increased interactions with the walls. The shapes of the reed's bending Modes 1 and 2 in each of the two channels (Figures III.3-8b and c) show that when the walls are farther apart, the first mode exhibits a simple curvature with no clear inflection points during the entire oscillation cycle. However, the second mode develops and inflection point at  $x/L \approx 0.5$  and a permanent node at  $x/L = 0.78$ . The first bending mode in the 5 mm channel is significantly different from Mode 1 in the 25 mm channel. Owing to the proximity of the walls, Mode 1 exhibits a permanent node at  $x/L = 0.56$ , and, moreover, shows attachment to the wall for  $x/L > 0.88$ . The

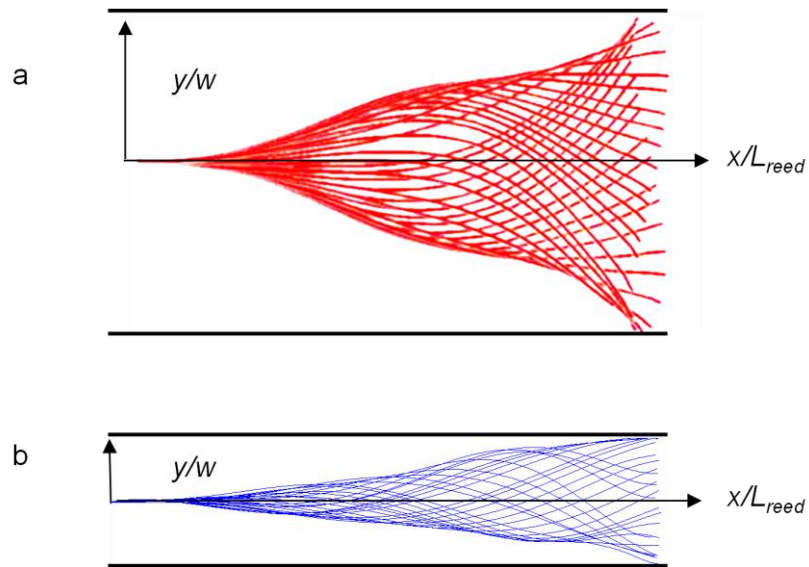


**Figure III.3-7.** Overlaid traces of the reed's centerline in the 25 mm ( $L = 45$  mm) (a) and 5 mm ( $L = 50$  mm) (b) channels just past the critical velocity (the reed thickness  $38 \mu\text{m}$  and its lengths in the 25 and 5 mm channels are 45 and 50 mm, respectively). The traces are acquired phase-locked to the passage of the tip of the reed at 39 equally-spaced positions across the width of the channel. The mean flow velocity in each of the channels is 5 m/sec.

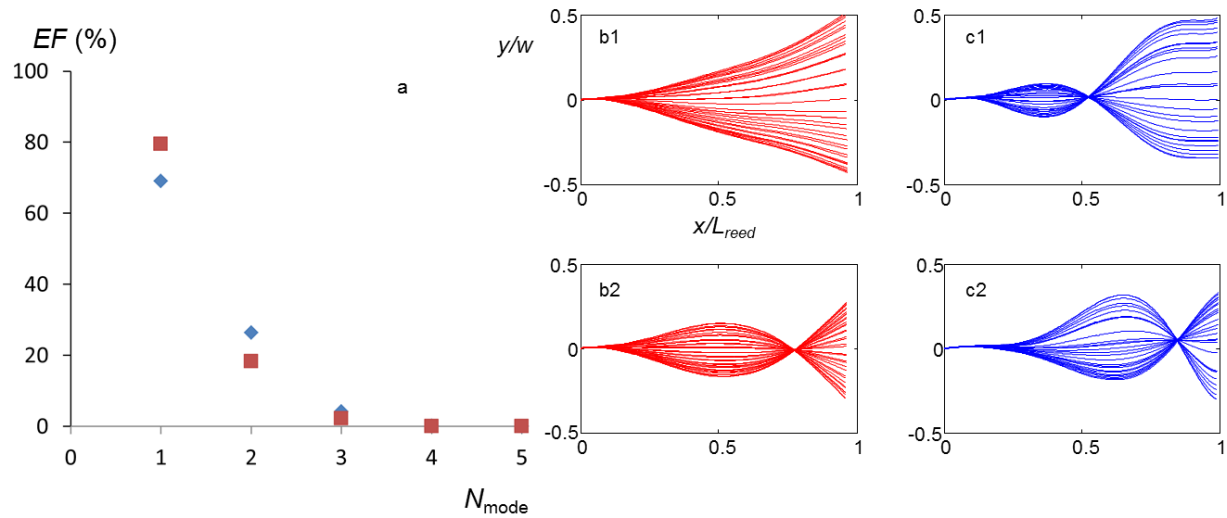


**Figure III.3-8.** Energy fraction in the first five POD modes of the reed in the 25 mm (■) and 5 mm (◆) channels (a), and POD modes 1 and 2 of the reed's centerline in the 25 (b1, b2) and 5 mm (c1, c2) channels (cf. Figure III.4-8).

shape of Mode 2 in the 5 mm channel is reasonably similar to the shape of Mode 2 in the 25 mm channel (Figures III.3b2 and c2) although the node of Mode 2 in the 5 mm channel migrates somewhat farther downstream (from  $x/L = 0.43$  in the 25 mm to  $x/L = 0.88$  in the 5 mm channel) and exhibits a somewhat higher amplitude compared to the width of the channel.

The kinetic energy of the reed is calculated using the motion of the (conditionally-averaged) centerline across the channel (neglecting spanwise variations). In these calculations the  $x$ - $y$  coordinates of a given point  $s$  along the reed (measured from its root) are computed for each of the 39 cross stream positions of the reed's centerline during the oscillation cycle. The kinetic energy of the reed elements ( $ds_{reed} = L/1000$ ) along  $s$  yields the distribution of kinetic energy along the reed. The present investigations demonstrated that the reed's kinetic energy  $KE_{reed} = \int 0.5 \rho_{reed} V_{reed}^2 th(ds_{reed})$   $KE_{reed} \approx O(10^{-7} J)$  and is typically four orders of magnitude higher than the elastic potential energy  $PE_{reed} = \int \frac{1}{24} Et^3 (y'')^2 dx$ . Variation of distributions of the reed's kinetic energy along its length during the oscillation cycle is compared using color raster plots for the two channel widths (25 and 5 mm) in Figures III.3-9a and b following the onset of the critical velocity (channel speed of 5 m/sec). The dashed lines correspond to the times when the tip of the reed first touches the sidewalls. Perhaps the most prominent feature of these distributions is the periodic build up and release of the kinetic energy at any position  $s$  along the reed that intensifies closer to the tip and is indicative of the effect of the interaction of and energy exchange between the flow and the reed. Of particular note is the temporal change in the tip kinetic energy as the reed moves from the center of the channel to its sidewalls. At the center of the channel, the kinetic energy has a local maximum, and the energy is lost as a result of either slowdown near or impact on the surfaces (the corresponding times are marked by the dotted lines). It is noted in passing that the motion and kinetic energy distribution of the reed in the 5 mm channel are somewhat asymmetric with respect to the channel's centerline as a result of stresses in the reed due to the laser cutting. Comparison between the kinetic energy of the reed in the 25 and 5 mm channels shows that for the same flow speed, the kinetic energy of the reed is significantly higher (the peak at the tip is 1.42 times higher in the 25 mm channel).



Although the respective tip oscillation frequencies in the 25 and 5 mm channels are about 50 and 100 Hz, the oscillation amplitude is 5 times higher in the former and therefore the kinetic energy is over 6 times higher. The variation with the channel Reynolds number of the reed's total kinetic energy (integrated along  $s$ )

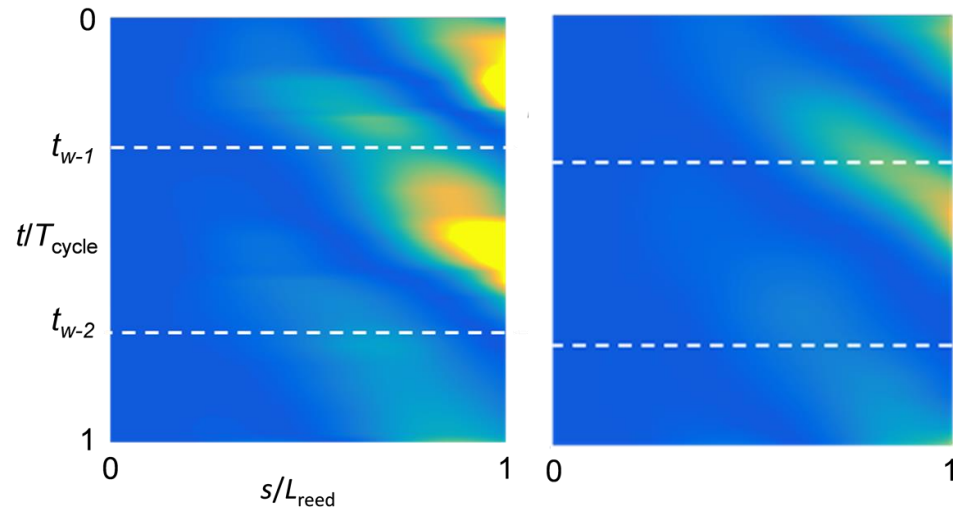


**Figure III.3-9.** Color raster plots of the variation of the reed's kinetic energy (per unit length) along its centerline length  $s$  during the nominal oscillation period  $T_{\text{cycle}}$  : a) 25 mm channel (  $L = 45$  mm,  $t = 38$  mm), and b) 5 mm channel (  $L = 50$  mm,  $t = 38$  mm). The times  $t_{w-1}$  and  $t_{w-2}$  correspond to the times at which the reed tip first touches the channels left (1) and right (2) side walls (cf. Figure III.4-1).

during the oscillation cycle is shown in Figure III.3-10a and b. These data are plotted so that the cycle begins at the time that the reed touches the surface of the sidewall. It is noted that even though the tip of the reed is at rest on the surface, the (total) kinetic energy is nonzero since the bulk of the reed is still moving. Another notable feature is that the cycle frequency is twice the oscillation frequency of the reed (due to the double-pass through the center). The total kinetic energy of the reed increases (Figure III.3-10) increases with Reynolds number although the increment from  $Re = 4,000$  to  $6,000$  is smaller than the increment from  $Re = 2,000$  to  $4,000$

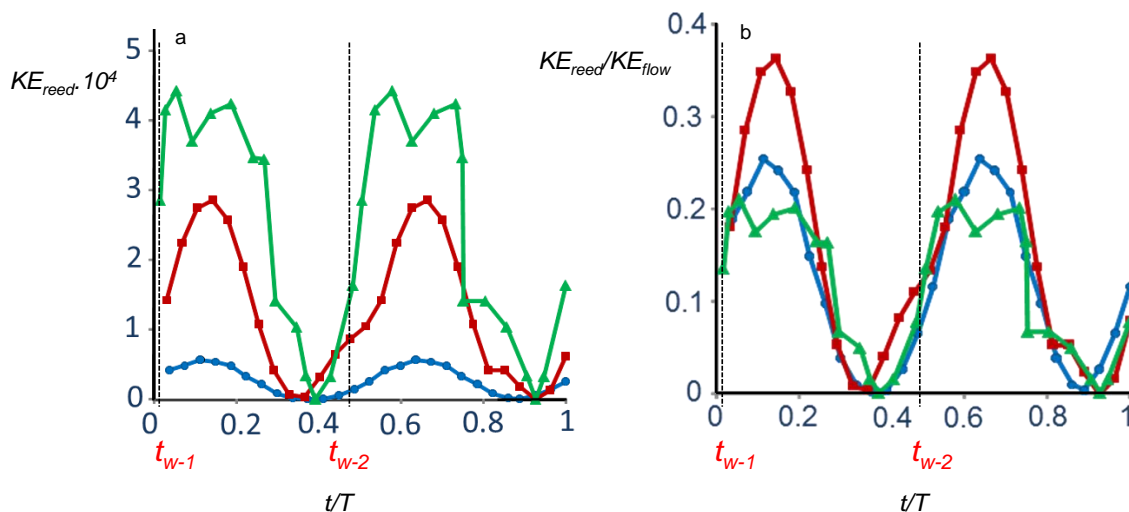


**Figure III.3-10.** Variation of the a) Total kinetic energy of the reed (integrated along  $s$ ) during the oscillation cycle, and b) Fractional kinetic energy (ratio of the kinetic energies of the reed and flow) for  $Re = 2,000$  (  $\bullet$  ),  $4,000$  (  $\blacksquare$  ) and  $6,000$  (  $\blacktriangle$  ). The times  $t_{w-1}$  and  $t_{w-2}$  (cf., Figure III.4-11) are marked for reference.

suggesting some saturation. The ratio between the kinetic energy of the reed and of the mean flow in the channel (Figure III.3-10b) is plotted in figure III.3-10b. As  $Re$  is increased from 2,000 to 4,000 the fractional kinetic energy of the reed increases,  $KE_{reed}/KE_{flow} = (S/U^2L) \int V_{reed}^2 ds_{reed}$  however, as  $Re$  is increased further to 6,000, the fractional kinetic energy transfer *decreases*. This can be attributed to the limitation that is imposed by the sidewalls on the motion of the reed as the flow  $Re$  increases that is manifested by larger areas of contact between the reed and the wall.

### III.3.3 Field Dynamics in the Presence of the Reed

The effects of the reed on the flow within the channel are depicted in power spectra of the streamwise velocity in the 25 mm channel that are measured downstream of the reed at  $x/w = 3.08$ , 5.08 and 7.08 (or at  $0.08w$ ,  $2.08w$ , and  $4.08w$  relative to the tip) at the channel's centerline and outside of its wall layer ( $0.08w$  from the wall) as shown in Figures III.3-11a and b, respectively for  $Re = 7,200$ . The power spectrum for  $x/w = 7.08$  measured just upstream from the channel's exit plane is compared with the spectra that are closer to the reed to emphasize the evolution of the spectral components within the flow. At  $x/w = 3.08$  on the centerline of the channel (Figure III.3-11a), the dominant frequency is the oscillation frequency of the reed (50 Hz) and the spectrum exhibits a large number of higher harmonics that also indicate higher oscillation modes of the reed. It is noteworthy that the spectral components at the fundamental frequency and its odd harmonics are lower in magnitude than the even harmonics. This spectral pattern is associated with the alternate shedding of vortical structures of decreasing scales during each passage of the tip of the reed across the width of the channel at twice the fundamental frequency and therefore the even harmonics represent the vortices advection and alternate interactions with the channel walls downstream of the tip of the reed. Comparison of the spectral distributions at  $x/w = 3.08$  and 7.08 (in grey) demonstrate that as the flow is advected to the exit plane of the channel, the magnitude of the harmonics that are associated with the motion and vortical shedding (over a broad range of scales) by the reed diminishes and the energy of these spectral components is distributed to other spectral components, and leads to a significant overall increase in the background spectral content. In fact, there is an increase of nearly a decade in the spectral content of the low-frequency end of the flow. *This is remarkable, because it means that energy from smaller scales (higher frequencies) is transferred to the lower frequencies within the flow, or down the energy cascade.* While at  $x/w = 5.08$  the spectral distribution demonstrates that a broad increase in the spectral content of the flow at the low frequencies is accomplished, there

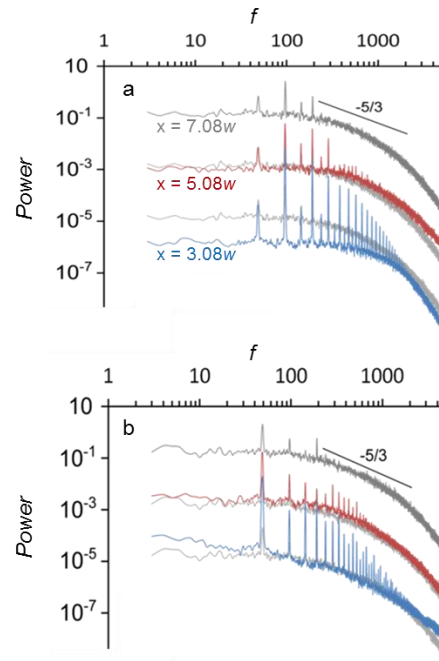


**Figure III.3-11.** Power spectra of the streamwise velocity measured along the channel's centerline (a) and just outside the wall boundary layer (b) at three streamwise stations:  $x = 3.08w$ ,  $5.08w$ , and  $7.08w$ . Each of the spectra at  $x/w = 7.08$  and  $5.08$  are shifted by two decades and the spectrum at  $x/w = 7.08$  is repeated for reference (in light grey).



is a significant further increase of the spectral content at the high frequencies ( $f > 250$  Hz) which is indicative of an increase in small-scale motions that are associated with mixing. These changes are accompanied by a reduction in the magnitude of the harmonics of the reed's frequency, which is especially pronounced at the high harmonics above 400 Hz indicating stronger transfer to small-scale motions. At the exit plane of the channel  $x/w = 7.08$  the spectrum contains four harmonics of the reed's oscillation frequency and exhibits a  $-5/3$  inertial subrange, which is indicative of significant turbulent characteristics despite the low Reynolds number of the flow ( $Re = 7,200$ ). It is also important to note that dissipation within the channel leads to some reduction in the energy of the small scale motions as is evident by the decrease in the magnitude of the small scales between  $x/w = 5.08$  and  $7.08$ , indicating that ultimately, the effects of the flow actuation by the reed's motion diminish due to dissipation within the background flow. The spectral measurements near the channel's wall ( $0.08w$  from the surface) in Figure III.3-11b demonstrate that the broad increase in the spectral content of the flow that is evident along the centerline is already present near the wall layer and that there is a relatively small change in the overall broad spectral levels between the spectra at the exit plane and at  $x/w = 3.08$  and  $5.08$ . This may be attributed to the strong, nominally time-periodic oscillations of the flow near the surface due to the interactions of the reed with the flow near the channel's walls. While the spectra near the surface exhibit the same content as at the centerline, the spectral magnitudes of the odd and even components are nearly uniform.

The interactions between the reed and the channel flow are assessed from position-locked PIV measurements (described in §III.3.1) within the cross stream ( $x$ - $y$ ) plane along the centerline of the channel over the reed's surface and downstream of its trailing edge. These data are taken at 39 preset cross stream positions of a reference point at the reed's midspan and  $0.1L$  upstream of its trailing edge, and includes 170 image pairs at each position. Each position-locked data set includes four streamwise varying partially overlapping (16%) fields of view each spanning the width of the channel and  $\Delta x = 0.67w$  long (the entire field of view is  $1.1 < x/w < 3.7$ ). The open-return flow channel was seeded with fog particles at a controlled concentration upstream of the diffuser (cf. 1). A separate CCD camera is triggered to simultaneously acquire images of the reed's centerline synchronized with the PIV images. Figure III.3-12 shows 18 color raster plots of spanwise vorticity concentrations superposed with velocity vectors over and downstream of a  $38\text{ }\mu\text{m}$  thick,  $45\text{ mm}$  long and  $23\text{ mm}$  wide polyester reed at the  $x$ - $y$  plane through centerline of the  $25\text{ mm}$  channel at  $Re = 7,000$  (the reed centerline is marked in red). Each image is characterized by a reference distance of near the tip of the reed to the channel's centerline. The sequence begins when the tip of the reed is at  $y/w = 0.35$  above the centerline near the top sidewall in Figure III.3-12i, and ends in Figure III.3-12xviii when the tip is at  $y/w = 0.3$  (the last position in this cycle) after the reed will have completed a full sweep across the channel.

The reed centerline primarily exhibits a first-order bending mode (cf. Figure III.3-8). The unstable oscillations of the reed clearly affect the flow on both its sides. In Figure III.3-12i, the constricted flow above the reed results in a jet-like flow that is characterized by the formation of two layers of spanwise vorticity of opposite sense that are formed at the surface of the top wall (CCW) and along the top surface of the reed (CW). The CCW vorticity along the wall leads to a significant thickening of the wall boundary layer while the "free" CW concentration rolls up to form a vortex that spans the full height of the channel before it is advected downstream. As the tip of the reed approaches the top surface ( $y/w = 0.45$ ), the jet flow is blocked and the reed sheds CCW vorticity from its bottom surface (in this orientation) that merges with the CCW vorticity

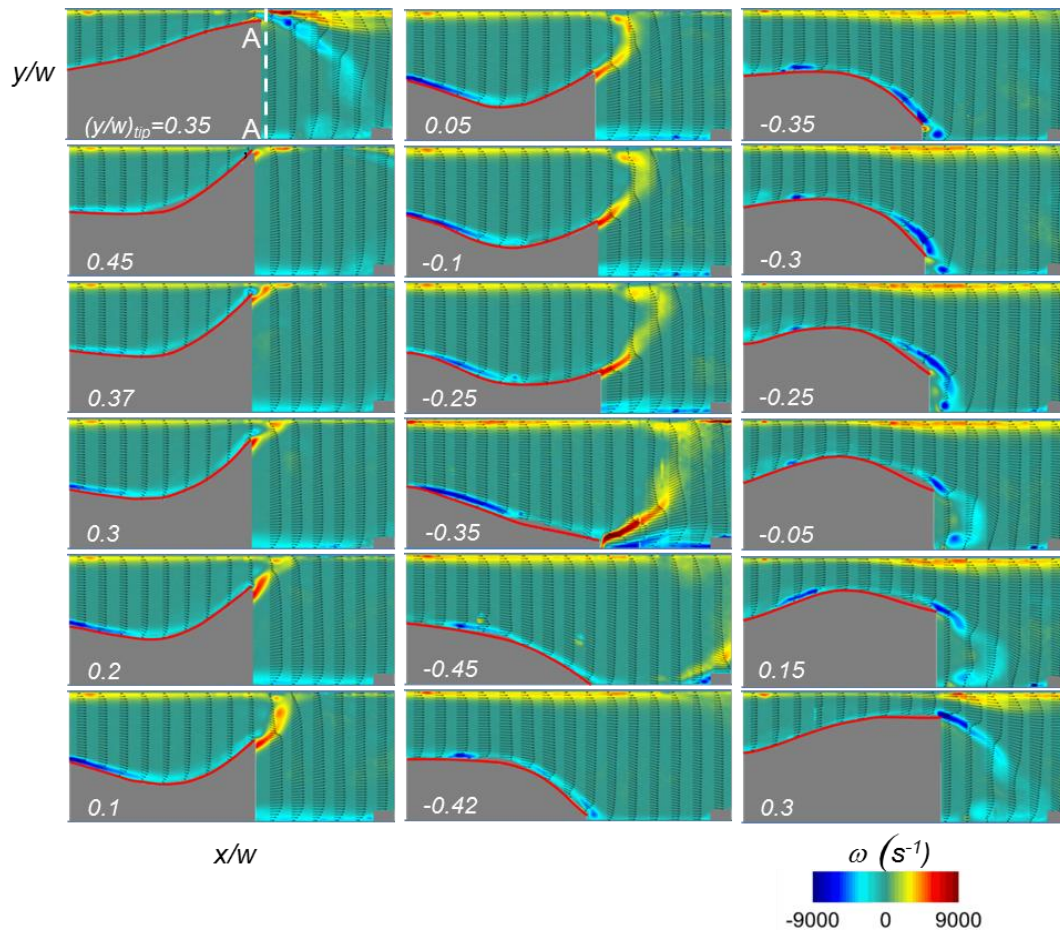


**Figure III.3-12.** Color raster plots of spanwise vorticity concentrations superposed with cross stream distributions of velocity vectors in the flow field above the reed and in its near wake in the  $x$ - $y$  centerplane of the 25 mm wide channel. The trace of the reed's centerline ( $t = 38$  mm,  $L = 45$  mm,  $W = 23$  mm) is also shown for reference, and the gray area underneath the reed marks the shadow domain. These images are acquired phase-locked to a series of 39 preset, equally-spaced cross stream positions of the reed's tip  $(y/w)_{tip}$  measured relative to the channel's center and noted at the bottom left side of each image.

in the wall layer downstream of the tip of the reed and disrupting the flux of CCW vorticity along the surface upstream of the tip of the reed. As a result of the buildup of pressure above the surface of the reed by the blocked flow and the lower static pressure on the bottom surface of the reed which also increases somewhat in the streamwise direction the reed bends towards the bottom surface upstream of its trailing edge, and begins to move towards the bottom surface of the channel (Figure III.3-12iii,  $y/w = 0.37$ ). As it is moving towards the bottom surface it continues to shed CCW vorticity from its bottom surface and, at the same time, the change in curvature and pressure gradient along its top surface leads to the formation of a layer of CW vorticity upstream of the concave bend on the top surface (Figures III.3-12iv-vi). As the reed continues its sweeping motion towards the bottom surface the layer of CCW vorticity begins to roll up and interact with the CCW vorticity layer on the top surface (Figures III.3-12vii-ix). It is remarkable that this interaction severs the surface vorticity layer resulting in thickening upstream of the interaction ostensibly as a result of the adverse pressure gradient that is imposed by the rolling vortex. This modulation of the CCW surface vorticity layer diminishes as the CCW vortex is advected downstream. As the reed approaches the bottom surface it leads to the

formation of another jet like flow in Figure III.3-12x ( $y/w = -0.35$ ), that is similar to the structure in Figure III.3-12i. When the flux of CCW vorticity from the bottom surface of the reed ceases, CW vorticity concentrations along the convex surface of the reed thicken by the slowing (diffusing) flow above the reed and the CW vorticity begins to shed and interact with the vorticity layer on the bottom surface (Figures III.3-12xiii-xvi) as the reed changes direction and moves towards the top surface ending up with acceleration and jet-like ejection of the constricted flow (Figure III.3-12xviii).

It is instructive to consider the vorticity flux in a cross stream boundary that extends across the width of the channel and includes the tip of the reed (Figure III.3-13). The cross stream variation of the flux ( $u\omega$ ) is plotted using color raster plots in unit strips that span the width of the 25 mm channel including the surfaces of the sidewalls (top and bottom) as a

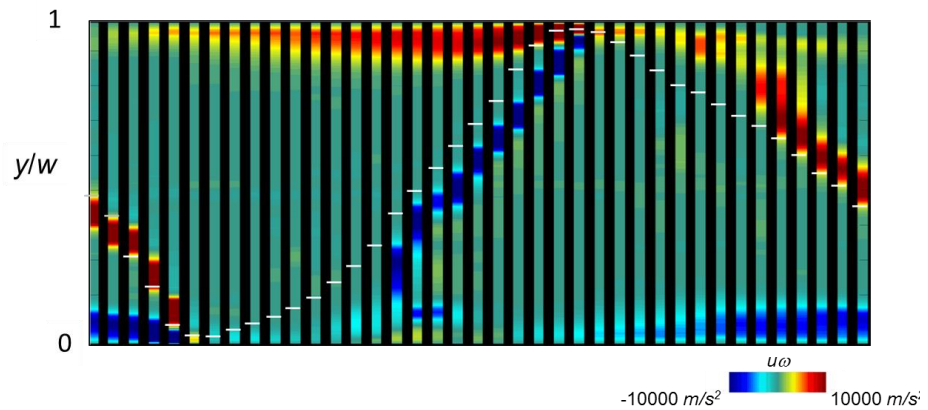


**Figure III.3-13.** Variation of the vorticity flux at the tip of the reed in the 25 mm channel as it moves across the channel width during a full oscillation cycle (the cross stream position of the reed is indicated by white dashes). The vertical color raster bar indicate the cross stream variation of the flux (the width of the bar is arbitrary) as a reference point  $0.1L$  upstream of the tip of the reed at its midspan passes at 39 positions across the channel width.

reference point on the reed (midspan,  $0.1L$  upstream of the tip) passes at each of 39 cross stream positions during the oscillation cycle. A white line segment marks the elevation of the reed at each unit flux strip. At the beginning of the cycle, the reed is sweeping towards the bottom surface and the flux is predominantly from the top surface of the reed leading to the rollup and formation of a CCW vortex that spans the width of the channel. As the reed approaches the bottom surface, the flux of CW vorticity along the surface is disrupted, and appears to be completely suppressed as the reed changes its direction and begins to move towards the top surface. As shown, the flux of vorticity along the bottom surface does not recover until the reed begins to move towards the bottom surface from the top, and therefore it is modulated at the oscillation frequency of the reed. As the reed moved towards the upper surface the vorticity flux is primarily from its surface that faces the bottom wall and leads to the formation of a CCW vortex. Similar to the bottom surface, as the reed reaches the top surface, it disrupts the flux of the CCW vorticity along the top surface. It is conjectured that this time-periodic, alternating disruption of the vorticity layers along the top and bottom surfaces can lead to significant enhancement in heat transfer as discussed in §III.3.4.

The effects of the counter-rotating nominally time-periodic vortical structures that are shed by the motion of the reed on the velocity field can be discerned from color raster plots of the velocity magnitude downstream of the reed in the 25 mm channel ( $1.7 < x/L < 5.6$ ) that are locked to four cross stream positions of the reed  $y/w_{tip} = 0.4, 0.05, -0.25$  and  $-0.4$ , in Figures III.3-14a-d, respectively (cf. Figure III.3-12). These data were acquired using five, partially

overlapping fields of view across the width of the channel, each  $1.33w$  long with streamwise overlap of 16%. These data show low-velocity cells that identify the “braids” region between successive counter-rotating vorticity concentrations that are shed from the reed as they are advected downstream (the advection is marked using dashed lines). The flow motions that are induced by these vortical structures result in transport of hot fluid from the surfaces and its mixing with the core flow for enhanced heat transport.

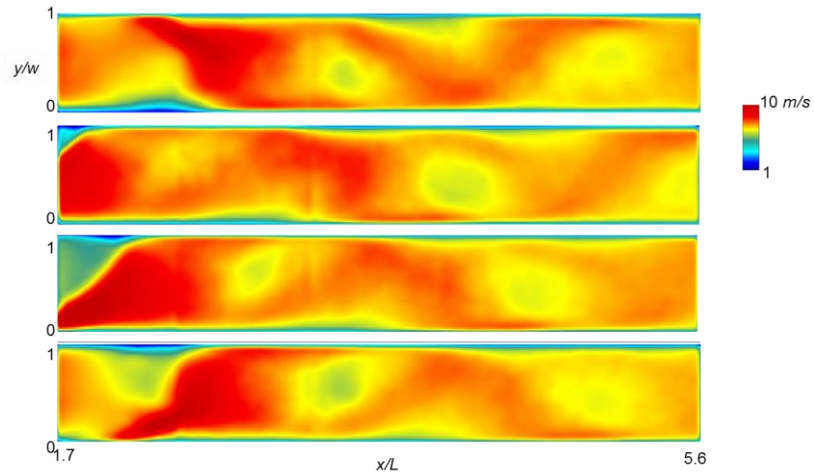


**Figure III.4-14.** Color raster plots of distributions of the velocity magnitude in the 25 mm channel downstream of the reed ( $1.7 < x/L < 5.6$ ) at four reed positions  $y/w_{\text{reed}} = 0.4$  (a),  $0.05$  (b),  $-0.25$  (c), and  $-0.4$  (d), (cf. Figure III.3-12).

The evolution of small scale motions and mixedness within the 5 mm channel is assessed from distributions of turbulent kinetic energy [ $TKE(y; x) = (u'^2 + v'^2)/2$ ] that is measured at 10 equally spaced stations in the streamwise domain  $18 < x/w < 47$  ( $1.8 < x/L < 5$ ) as shown in Figures III.3-15a-f. In the absence of the reed, the natural evolution of the flow shows extremely low concentrations of  $TKE$  (and therefore low heat transfer) at  $Re = 2,000$  (Figure III.3-15a) through the downstream end of the channel. While these data do not capture the (secondary) corner

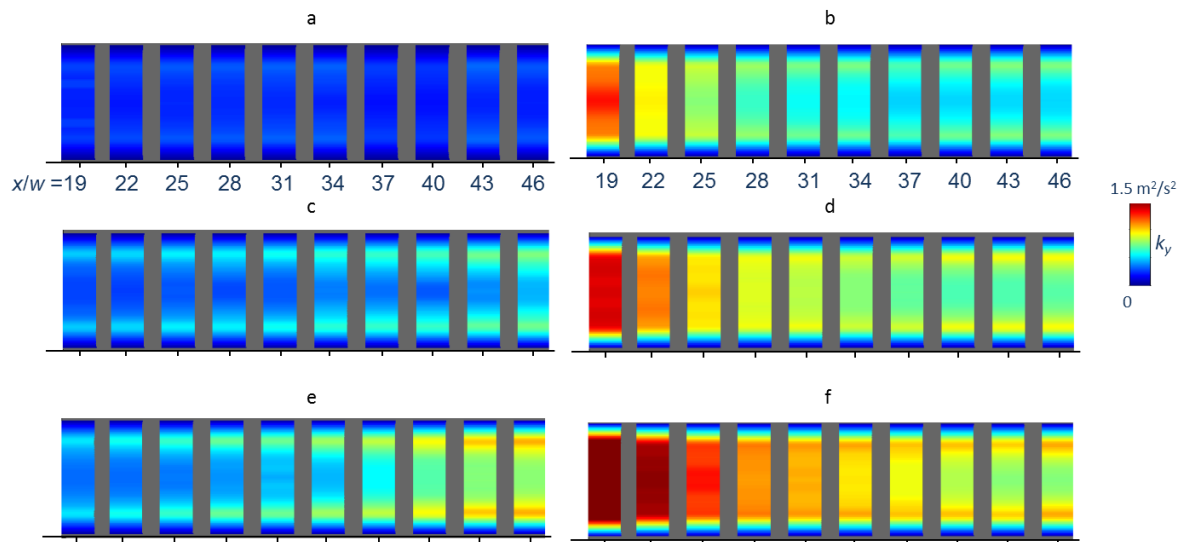


**Figure III.4-15.** Strips (measuring  $1 \times 2.6 w$ ) of color raster plots of cross stream distributions of the turbulent kinetic energy  $TKE$  measured using PIV in the absence (a, c, and e) and presence (b, d, and f) of the reed within the 5 mm channel for  $Re = 2,000$  (a, b),  $4,000$  (c, d), and  $6,000$  (e, f). The distributions of the  $TKE$  are measured at 10 equally spaced streamwise stations  $18 < x/w < 47$  ( $1.8 < x/L < 5$ ). Each distribution is uniform across the width of the strip, centered around the streamwise location of the measurement, and spans the height of the channel.



flows, it appears that small-scale motions are nearly absent at this pre-transition  $Re$ . As the Reynolds number is increased to 4,000 (Figure III.3-15c), the base flow exhibits concentrations of  $TKE(y; x)$  that begin outside of the wall layers on both sides of the channel (and are already present at  $x/w = 19$ ) and undergo cross-stream spreading towards the center of the channel farther downstream. It is remarkable that these concentrations of  $TKE$  do not appear to spread into the developing boundary layer over the side wall surfaces of the channel. The appearance of these small-scale motions might be associated with an inviscid shear-layer instability associated with inflection points of the velocity distribution away from the surface ( $y/w \approx 0.2$ ) at the elevated  $Re$ . At  $Re = 6,000$  (Figure III.3-15e),  $TKE(y; x)$  is intensified in these external layers (above the sublayer domain of the wall boundary layers) and within the core flow indicating faster formation and presence of small-scale motions. The evolution and distributions of  $TKE(y; x)$  in the presence of the reed are remarkably different (Figures III.3-15b, d, and f). To begin with, the  $TKE$  is substantially intensified downstream of the tip if the reed owing to the nominally time-periodic shedding of counter-rotating small scale vortical motions. The data also shows that  $TKE(y; x)$  strengthens significantly with increasing Reynolds number as the receptivity of the base flow to the imposed disturbances increases, but the low  $Re$  of the base flow also leads to significant dissipation of the flow disturbances that are imposed by the reed. For  $Re = 2,000$  (Figure III.3-15b), the rate of decay of the imposed disturbances is higher near the centerline and reaches the levels of the external wall layer at the measurements station  $x/w = 34$ , but the decay within the shear layer appears to be significantly slower and the imposed perturbations persist through the downstream end of the test section. These the streamwise effect of the reed on the core flow nearly doubles (at the centerline) between  $Re = 2,000$  and 4,000 (Figure III.3-15d). It is noteworthy that despite the dissipation on the centerline  $TKE(0; x)$  at  $x/w = 25$  at  $Re=2,000$ , is reached at  $x/w = 34$  at  $Re=4,000$ , and  $x/w = 43$  at  $Re = 6,000$  (Figure III.3-15f). Another important attribute of the reed actuation is that  $TKE$  increases within the wall (sub) layers compared to the base flow (compare Figures II.4-14a, c, and e to b, d, and f), indicating the potential for enhanced heat transfer at the surface sublayer, and then mixing within the core flow.

The streamwise development of the flow in the channel is characterized using cross stream integral measures namely, the integrated turbulent kinetic energy  $\overline{TKE}(x)$  and the corresponding shape factor  $\alpha(x)$  of the streamwise velocity distributions ( $\alpha = \int_0^w \left(\frac{u}{U}\right)^3 d\left(\frac{y}{w}\right)$ ) in the center plane of the channel (Figure III.3-16a and b, respectively). Velocity measurements across the width of the channel are taken using PIV at discrete streamwise stations in the absence and presence of the reed. In the absence of the reed there are 14 equally-spaced streamwise positions (11 in

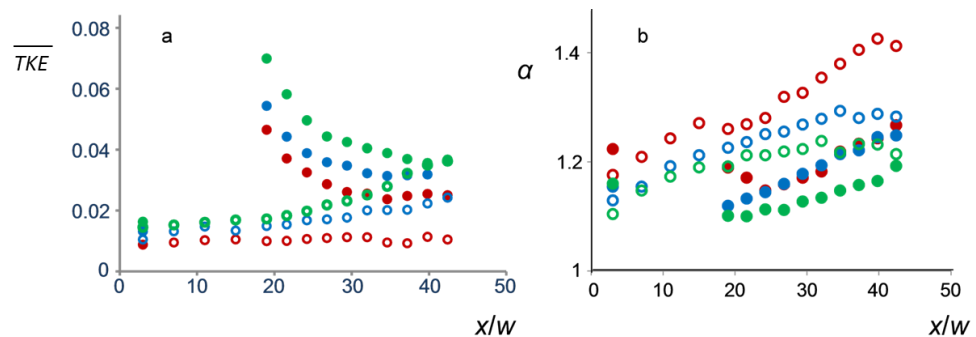


**Figure III.4-16.** Streamwise Variation of the cross stream integrated  $\overline{TKE}(x)$  (a), and the integral shape factor of the streamwise velocity  $\alpha(x)$  in the absence (open symbols) and presence (closed symbols) of the reed:  $Re = 2,000$  ( $\circ, \bullet$ ),  $Re = 4,000$  ( $\circ, \bullet$ ) and  $Re = 6,000$  ( $\circ, \bullet$ ).

the presence of the reed). In the absence of the reed  $\overline{TKE}(x)$  is nearly invariant at  $Re = 2,000$ , and at  $Re = 4,000$  and  $6,000$  the  $\overline{TKE}(x)$  is nearly invariant (although higher with  $Re$ ) through  $x/w \approx 30$  where it begins to increase at a streamwise rate that appears to increase with  $Re$  owing to natural transition. In the presence of the reed,  $\overline{TKE}(x)$  is nearly the same as that of the base flow upstream of the reed ( $x/w = 15$ ) but there is a large increase downstream of the reed where the magnitudes of  $\overline{TKE}(x)$  increase with  $Re$ , and are up to 3.5 times larger than the corresponding magnitudes in the base flow. These data show that  $\overline{TKE}(x)$  decays in the streamwise direction at a rate that appears to be independent of  $Re$ , and reaches an asymptotic level within the channel. While the levels for the base flow and in the presence of the reed at  $Re = 6,000$  are nearly the same at the downstream end of the channel, the corresponding levels of the base flow  $\overline{TKE}(x)$  are significantly smaller than in the presence of the reed indicating that the attenuation associated with dissipation does not completely erase the effect of the actuation by the reed. *As shown in connection with Figure III.3-18, even though  $\overline{TKE}(x = L)$  in the absence and presence of the reed at  $Re = 6,000$  reach a similar magnitudes, the heat transfer in the presence of the reed is about two times higher than in the base flow at the same  $Re$ .* Similarly,  $\overline{TKE}(x = L)$  at  $Re = 2,000$  and  $4,000$  in the presence of the reed is considerably higher than in the base flow indicating extended potential for enhanced cooling at lower  $Re$ . A second integral scale that measures the performance of the reeds is the velocity shape factor  $\alpha(x)$  in Figure III.3-16b. The shape factor measures the deviation of a given velocity distribution from a uniform velocity for which  $\alpha = 1$  (in a turbulent flow  $\alpha \sim 1.1-1.3$  and for a parabolic profile  $\alpha = 2$ ). In the base flow,  $\alpha(x)$  increases nearly monotonically in the streamwise direction as the flow evolves from entrance flow to a channel flow. For a given streamwise location  $\alpha(x)$  decreases with  $Re$  since the flow becomes transitional, and for  $Re = 4,000$  and  $6,000$   $\alpha(x)$  has a local maximum near  $x/w \approx 35$  and then begins to decrease indicating the onset of transition to turbulence. In the presence of the reed,  $\alpha(x)$  decreases significantly compared to its magnitude in the base flow at the same  $Re$  indicating velocity distributions that have a more pronounced turbulent character. The monotonic increase in  $\alpha(x)$  downstream of the reed is associated with the dissipation and the streamwise decrease  $\overline{TKE}(x)$  with reed actuation.

### III.3.4 Heat Transfer Measurements

The effect of the reed on heat transfer in the 5 mm channel is assessed using sidewalls with integrated film heaters (operating in constant heat flux, cf, §III.3.1). The heat flux to the heaters was varied over a range of flow rates ( $2,000 < Re < 10,000$ ) such that the maximum initial temperature difference  $ITD(x) = T_{wall}(x) - T_{in}$  for both the base flow and in the presence of the reeds was  $60^\circ\text{C}$ . Figures III.3-17a-c show the streamwise variation of  $ITD(x)$  at  $Re = 2,000$ ,  $4,000$  and  $6,000$  for the base flow and in the presence of 30 and 50 mm long reeds. In the base flow,  $ITD(x)$  increases monotonically, reaches a maximum  $ITD_{max} = 60^\circ\text{C}$  at  $x/w \approx 40$ , and thereafter decreases towards the free end of the channel. The present measurements show that the base flow dissipates 9.9 W, 15.7 W and 19.5 W at  $Re = 2,000$ ,  $4,000$  and  $6,000$  respectively. In the presence of the reeds  $ITD(x)$  immediately downstream of the reed decreases compared to the base flow (at  $Re = 2,000$   $\Delta ITD = 5.5$  and  $4.8^\circ\text{C}$ , for  $L_{reed}/w = 6$  and  $10$ , respectively, and at  $Re = 6,000$   $\Delta ITD = 3.3$  and  $2.3^\circ\text{C}$ , for  $L_{reed}/w = 6$  and  $10$ , respectively). It is noteworthy that while at  $Re = 2,000$  the change in the ITD is nearly independent of the length of the reed, the appearance of higher modes as the flow speed increases ( $Re = 6,000$ ) leads to higher ITD with the longer reed (at  $x/W = 6.5$ ) than in the base flow, but the wall temperature in the presence of the reed decreases significantly below the base flow for  $x/w > 20$ . These changes are clearly associated with

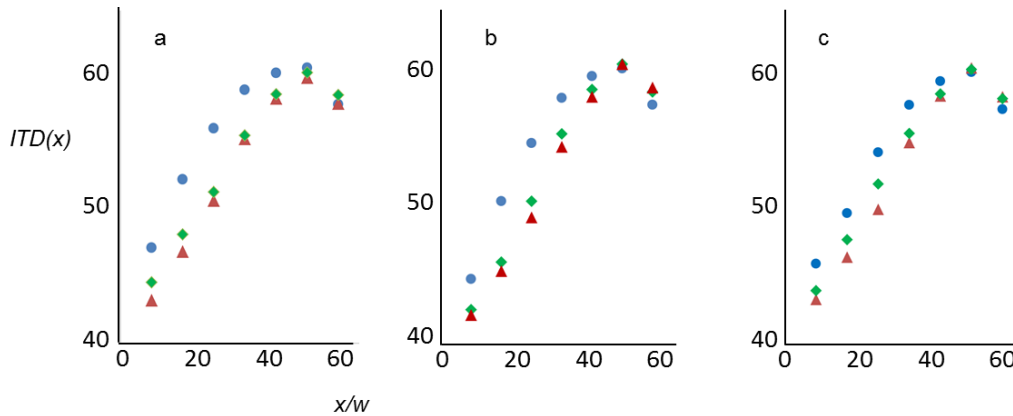


**Figure III.4-17.** Streamwise distributions of the channel wall temperature difference  $ITD(x) = T_{wall}(x) - T_{in}$  in the base flow ( $\bullet$ ), and in the presence of 30 ( $\blacklozenge$ ) and 50 ( $\blacktriangle$ ) mm long reeds. The maximum wall temperature difference,  $ITD_{max}$  was kept constant for all the experiments.

reduction in the wall-to-air thermal resistance downstream of the reed which persists through most of the length of the channel through  $x/w < 40$ , and beyond that the  $ITD$  in the presence of the reed is equal to the  $ITD$  of the base flow at all Reynolds numbers. This equality is more indicative of the thermal conditions at the free end of the channel rather than of the effective streamwise range of the reed actuation. It should be noted that while the difference in  $ITD(x)$  between the base and actuated flows are larger at  $Re = 2,000$ , the increment in heat dissipation at  $Re = 6,000$  is significantly higher. The respective power dissipation at the same maximum  $ITD(x)$  at  $Re = 2,000$ , 4,000 and 6,000 in the base flow are 9.9, 15 and 19.5 W, while with the reeds they are 16.6, 30.2 and 41 W (30 mm reed), and 16.9, 31.0 and 42.1 W (50 mm reed), i.e., up to a . The measurements show that the differences in power dissipation between the 30 and 50 mm reeds are rather small (1.8%, 2.6 and 2.7% higher for the longer reed at the same  $Re$  respectively).

A miniature thermocouple sensor and pitot tube mounted on a micrometer traverse were used to measure distributions of the flow temperature and speed at the exit plane of the 5 mm channel. The total heat flux through the channel  $\dot{Q} = \dot{m}C_p(T_{m,e} - T_{m,i})$  was computed using the mass flow rate  $\dot{m}$ , and the bulk mean temperatures of the flow at the channel's exit and inlet planes  $T_{m,e}$  and  $T_{m,i}$ , respectively.  $T_{m,e}$  is defined in equation III.3.4.2 as

$T_{m,e} = \int_0^w uTdy / \int_0^w udy$ . These data were used to compute the heat transfer coefficient  $h = \dot{Q} / [A(LMTD)]$  where  $A$  is the surface area of the channels and  $LMTD$  is the logarithmic mean temperature difference  $LMTD = (\Delta T_{w,i} - \Delta T_{w,e}) / \log_e \frac{\Delta T_{w,i}}{\Delta T_{w,e}}$  and  $\Delta T_{w,i}$

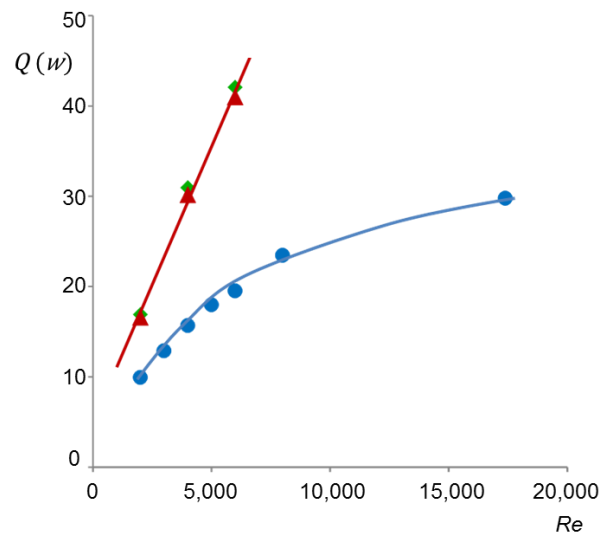


**Figure III.4-18.** Variation of overall power removed by the air with Reynolds number for base flow ( $\bullet$ ), and with the reeds:  $L = 30$  mm ( $\blacklozenge$ ), and 50 mm ( $\blacktriangle$ ).

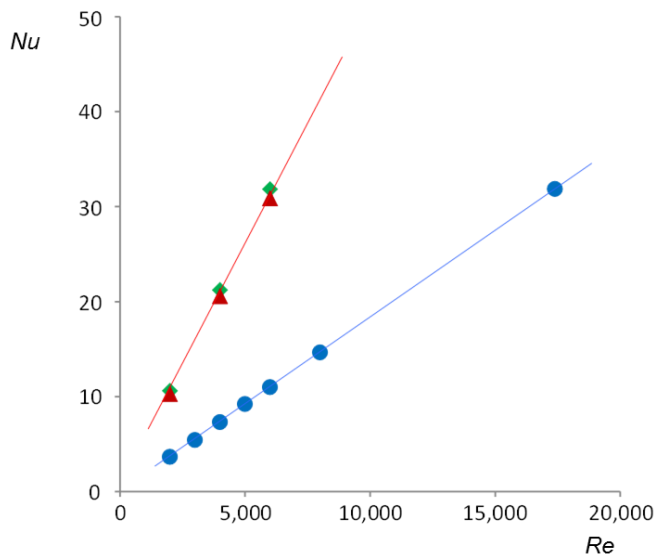


**Figure III.4-19.** Variation of average Nusselt number in the channel with Reynolds number for base flow (●), and with the reeds:  $L = 30$  mm (◆), and  $50$  mm (▲).

and  $\Delta T_{w,e}$  are the differences between wall temperature and air bulk mean temperature at the inlet and exit planes. Figure III.3-18 shows the variation of the power removed by the air,  $\dot{Q}$ , with  $Re$  in the channel. For the base flow,  $\dot{Q}$  increases linearly with  $Re$  (up to  $Re \sim 6,000$ ) and the rate of increase diminishes as  $Re$  is increased further, indicating the change in heat transfer as the flow becomes turbulent. In the presence of the reeds, however the rate of increase of  $\dot{Q}$  with  $Re$  is considerably higher and at least within the tested range does not seem to decrease as  $Re$  increases which is consistent with the enhanced  $TKE$  in the presence of the reeds (cf., Figure III.3-15). It is remarkable that apart from the fact that presence of the reed leads to enhanced heat transfer in the

channel at low  $Re$ , the enhancement of heat transfer persists and increases with  $Re$  compared to the base flow. These data also show that the power removed is relatively insensitive to the length of the reed, and therefore shorter reeds could be used to reduce the pressure drop in the channel. Figure III.3-19 shows the variation with  $Re$  of the Nusselt number,  $Nu = hD_h/K$ , ( $D_h$  is the hydraulic diameter of the channel and  $K$  is the thermal conductivity of air at the mean wall temperature) for the base flow and in the presence of short and long reeds. These data show that the rate of increase of  $Nu$  with  $Re$  is significantly higher in the presence of the reed exhibiting a distinct divergence between the two curves. This indicates that even though the turbulence level in the base flow increases with  $Re$ , the effect of the reed on the heat transfer increases even faster suggesting that the presence of the natural small-scale motions actually enhances the interactions of the reed with the flow and therefore its thermal performance. These measurements also show that the increase in  $Nu$  in the presence of the reeds is 178, 182, and 181% at  $Re = 2000$ , 4,000, and 6,000, respectively. By comparison, longitudinal rows of vortex generators that were used by Tiggelbeck et al. (1991), in a channel of the same aspect ratio and nearly similar  $L/W$  and yielded a maximum increase in the average  $Nu$  of 69% at the same  $Re$  while, the increase in pressure drop varied between 60% and up to 160%. The use of dimpled/protrusion channels used by Mahmood et al. (2001) or Elyaan et al. (2008) yielded increases in  $Nu$  of up to 150% at a  $Re_{D_h} = 5,000$ , but the increase in friction coefficient relative to the base channel was 3.5- to 5.5-fold larger.

While the introduction of reeds leads to a significant enhancement in the heat removed by the air  $\dot{Q}$ , there is also a corresponding penalty in increased pressure drop  $\Delta p$ . The thermal enhancement that is enabled by reed actuation is quantified using the coefficient of performance  $COP = P_{heat}/P_{fluid}$  or the ratio of the dissipated heat power to the invested fluid power, where  $P_{fluid}$  is determined using the flow's pressure drop  $\Delta p$ . The improvement in  $COP$  with reed actuation is compared to the base flow for maximum heat dissipation without exceeding a given



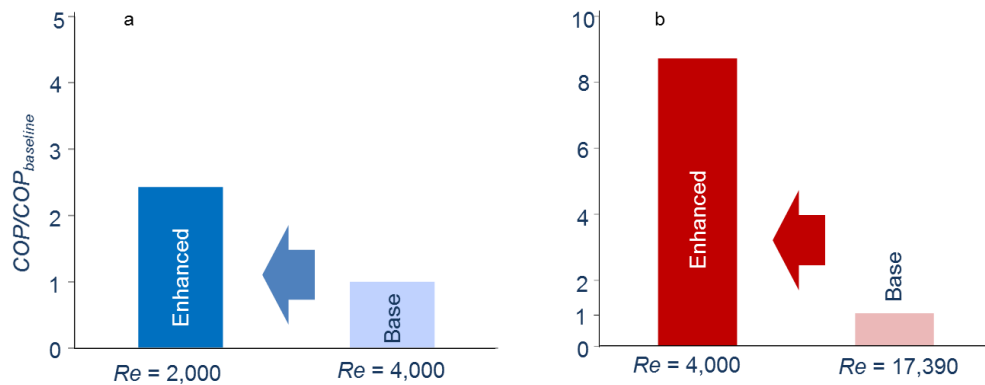


**Figure III.4-20.** Improvement in the COP over the base flow, and reduction in mass flow rate in the presence of reed: a) between  $Re = 4,000$  and  $2,000$  (increase in COP 1.5 times, mass flow rate 50%), and b) between  $Re = 17,390$  and  $4,000$  (increase in COP 9 times, and mass flow rate 77% ).

maximum wall temperature ( $80^{\circ}\text{C}$ ). The comparison between the base and reed-actuated flows is made at the same heat transfer while maintaining nominally similar wall temperature distributions by adjusting the flow rate in the channel (the flow rate required for the same heat dissipation in the presence of the reed is lower). Figures III.3-20a and b show the COP enhancement ( $COP/COP_{baseline}$ ) for low and high  $Re$ . The results show that the reed-enhanced COP increases with channel  $Re$  as might be expected given the changes in  $Nu$  in Figure III.3-19. For the lower range of  $Re$  (Figure III.3-20a), the COP enhancement is about 2.4-fold with a reduction in channel flow rate of 50% relative to the same heat transfer in the base flow. Similarly, at a higher range of  $Re$  (Figure III.3-20b), the enhancement in COP is about 9-fold in the presence of the reed with a corresponding reduction of 77% in flow rate compared to the base flow. This enhancement in COP as  $Re$  increases is apparent from figure III.3-18. The divergence between the power dissipation in the base flow and in the presence of the reeds indicates that the increase in channel Reynolds number that is necessary to accommodate a given power dissipation results in higher pressure drop and lower performance as compared to operation in the presence of the reed.

### III.4 Concluding Remarks

The synergistic research approach that has been employed in the current project is captured in Figure III.4-21. The experiments at Georgia Tech were conducted closely and in concert with simulations and modeling at Johns Hopkins University and with the inviscid modeling at University of Michigan to comprehensively explore the fluid physics and coupled structural dynamics of the complex aeroelastic interactions between reed. The combined experimental-modeling approach has yielded a comprehensive assessment of the factors that play an important role in determining the flutter boundary of for the reed. For example, Figure III.4-21 depicts the stability boundaries of the reed as measured in the experiments and predicted by the inviscid analysis and by the FSI simulations in terms of two key parameters, namely the reduced critical velocity  $U^*$  and mass ratio  $M^*$  (cf., §§III.1, III.2, and III.3). It is noteworthy that while the Reynolds number is clearly an important parameter for heat transfer, beyond a Reynolds number of about 500, this parameter does not play an important role in determining the flutter boundary. Finally, the present investigations demonstrated that confinement ratio plays a minor role in flutter instability unless the confinement become significant.

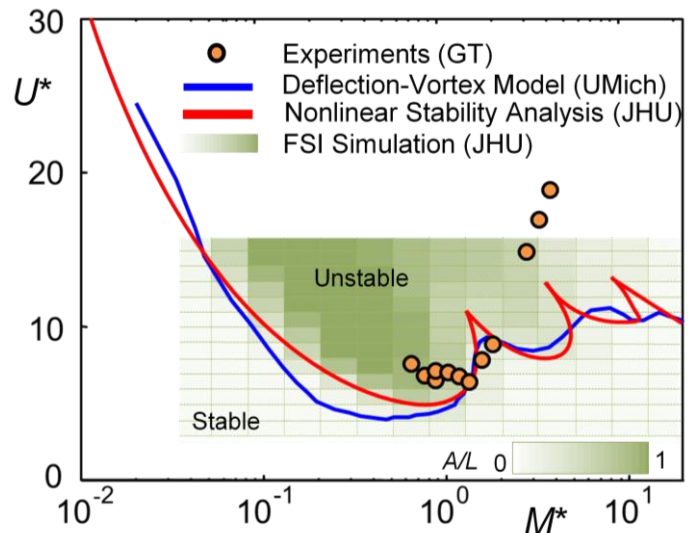


**Figure III.4-21.** Prediction of stability boundaries for the reed in channel from the various approaches employed in the current project.

The present investigations also focused on the mechanisms of the formation, shedding, and advection of a hierarchy of small-scale vortical motions that are effected by the aeroelastically fluttering reed at low (laminar or transitional) Reynolds numbers in simulations and experiments. Formation and advection of vorticity concentrations along the surface of the reed are induced by concave/convex surface undulations associated with its structural vibration modes that lead to alternate time-periodic shedding of CW and CCW vortical structures having cross stream scales that are commensurate with the cross stream amplitude of the reed motion and scale with the channel's width. The evolution of these vortices in the vicinity of the reed is strongly affected by interactions with the wall boundary layers that engender vorticity filaments spanning the entire height of the channel. These reciprocal interactions between the reed and the embedding channel flow lead to the evolution of small scale motions of decreasing scales that is characterized by enhanced dissipation and a distribution of spectral components that are reminiscent of a turbulent flow even at the low Reynolds number of the base channel flow. The reed's impact on the surface is accompanied by transitory vorticity shedding coupled with a local increase in the turbulent kinetic energy that result in strong increase in heat transfer. The reciprocal interactions between the reed dynamics and the channel flow link the kinetic energy of the reed to strong enhancement of the heat transfer (e.g.,  $Nu$ ) relative to the base flow. It is shown that the reed-induced heat transfer increases with  $Re$ , and results in significant improvement in the global thermal coefficient of performance (COP). It was also shown that while certain vortex configurations enhance heat transfer, they can also increase viscous dissipation, and the overall

thermal efficiency is a balance between these two opposing effects. The presence of the fluttering reed in a heated channel can lead to a 2-3 fold increase in the Nusselt number relative to the base flow for  $Re < 6,000$ . Furthermore, *the channel's thermal coefficient of performance (COP) is enhanced by 2.4-fold and 9-fold for base flows at  $Re = 4,000$  and  $17,400$ , respectively with corresponding decreases in the required flow rates of 50 and 77%.* These improvements can be leveraged to enhance cooling rates or to reduce flows rates and/or the size of conventional heat sinks.

The present project also led to the development of computational and experimental tools. Three distinct computational tools have been developed to support this research: *i.* Immersed boundary based coupled flow-structure-thermal solver for both two- and three dimensional configurations (Shoele & Mittal, 2015); *ii.* Inviscid fluid-structure interaction model (Alben, 2015); and *iii.* Inviscid, non-linear eigenvalue analysis model (Shoele & Mittal, 2016). The experimental methods have included development of novel measurement technologies of the reed-induced flow field. In particular, since the reed motion is only nominally-time-periodic and can change from one cycle to the next, measurements of the spatial position of the reed's surface and velocimetry of the ensuing flow field are triggered by its absolute position relative to the channel's walls (cf. §III.3). In addition, the present program, also provided insight into the reed's dynamics and technologies for its fabrication and mounting. It is anticipated that these tools will have wide applicability for a variety of research projects of relevance to DoD including thermal management (electronic cooling, condenser design), aeroelastic flutter, micro-aerial vehicles, and energy harvesting.

## REFERENCES

1. Agostini, B., Fabbri, M., Park, J. E., Wojtan, L., Thome, J. R. and Michel, B. "State of the art of high heat flux cooling technologies," *Heat Transfer Eng.*, **28**, 258–8, 2007.
2. Alben, S. "Flag flutter in inviscid channel flow," *Phys. Fluids*, **27**:033603, 2015.
3. Alben, S. "The flapping-flag instability as a nonlinear eigenvalue problem," *Physics of Fluids*, **20**:104106, 2008.
4. Alben, S. "Wake-mediated synchronization and drafting in coupled flags," *Journal of Fluid Mechanics*, **641**:489–496, 2009b.
5. Alben, S. and Shelley, M.J, "Flapping states of a flag in an inviscid fluid: Bistability and the transition to chaos," *Phys. Rev. Lett.*, **100**:074301, 2008.
6. Alben, S., "Simulating the dynamics of flexible bodies and vortex sheets," *J. Comp. Phys.*, **228**(7):2587–2603, 2009a.
7. Audoly, B. Pomeau, Y., "Elasticity and geometry," Oxford Univ. Press, 2010.
8. Bar-Cohen, A. and Iyegar, M. (2002) Design and Optimization of Air-Cooled Heat Sinks for Sustainable Development, *IEEE Transactions on Components and Packaging Technologies*, **25**, 584-591.
9. Bhardwaj, R. and Mittal, R., "Benchmarking a Coupled Immersed-Boundary-Finite-Element Solver for Large-Scale Flow-Induced Deformation." To appear *AIAA J.*, 2012.
10. Biswas, G., K. Torii, et al., "Numerical and experimental determination of flow structure and heat transfer effects of longitudinal vortices in a channel flow." *International Journal of Heat and Mass Transfer*, **39**(16): 3441, 1996.
11. Choi, H. and Moin, P., "Effects of the computational time step on numerical solutions of turbulent flow," *J. Comput Phys.* **113**, 1-4, 1994.
12. Crighton, D.G. "The Kutta condition in unsteady flow," *Ann. Rev. Fluid Mech.*, **17**(1):411-445, 1985.
13. D'Alessio, S.J.D., Steady and unsteady forced convection past an inclined elliptic cylinder. *Acta Mechanica* 123, 99-115, 1997.
14. Doaré, O., Sauzade, M. and Eloy, C., "Flutter of an elastic plate in a channel flow: confinement and finite-size effects," *Journal of Fluids and Structures*, **27**(1), 76-88, 2011.
15. Drofenik U., Laimer G. and Kolar J. W., "Theoretical Converter Power Density Limits for Forced Convection Cooling," *Proc. of the Int. PCIM Europe 2005 Conf.*, Nuremberg (Germany), June 2005, pp. 608-619, 2005.
16. Eloy, C., Souilliez, C. and Schouveiler, L., "Flutter of a Rectangular Plate," *J. Fluids and Structures*, **23**, 904–919, 2007.
17. Elyyan, M. A., Rozati, A., and Tafti D.K., "Investigation of Dimpled Fins for Heat Transfer Enhancement in Compact Heat Exchangers," *Int. J. Heat Mass Transfer*, **51**, 2950-2966, 2008.
18. Fua W-S and Tonga B-H., "Numerical Investigation of Heat Transfer of a Heated Channel with an Oscillating Cylinder," *Numerical Heat Transfer, Part A: Applications*:**43**(6), 2003.
19. Gee, D.L. and Webb, R., "Forced convection heat transfer in helically rib-roughened tubes," *Int. J. Heat Mass Transfer.*, **23**, 1127-1136, 1980.
20. Gerlach, D. W., Gerty, D., Mahalingam, R., Joshi, Y. K., Glezer, A., "A Modular Stackable

- Concept for Heat Removal From 3-D Stacked Chip Electronics by Interleaved Solid Spreaders and Synthetic Jets," *IEEE Transs Adv Packaging*, **32**, 431-439, 2009.
21. Gillespie, M. B., Black, W. Z., Rinehart C. S., and Glezer, A., "Local Convective Heat Transfer from a Constant Heat Flux Flat Plate Cooled by Synthetic Air Jets," *Journal of Heat Transfer*, **128**, 990-1000, 2006.
  22. Glauert, H. *The Elements of Airfoil and Airscrew Theory*. Cambridge Univ. Press, Cambridge, 1947.
  23. Goldberg, D.E., "Genetic Algorithms in Search Optimization and Machine Learning," *Addison Wesley*, P. 41, 1981.
  24. Goldstein, D., Handler, R. and Sirovich, L., "Modeling a no-slip flow boundary with an external force field," *J. Comput. Phys.*, **105**, 354-366, 1993.
  25. Greengard, L. "Potential flow in channels," *SIAM journal on scientific and statistical computing* 11 (4), 603–620 1990.
  26. Guo, C. Q & Paidoussis, M. P., "Stability of rectangular plates with free side-edges in two-dimensional inviscid channel flow". *Journal of Applied Mechanics*, **67** (1), 171–176, 2000.
  27. Hardin R. H. and Sloane, N. J. A. "A New Approach to the Construction of Optimal Designs", *Journal of Statistical Planning and Inference*, **37**, pp. 339-369, 2003.
  28. Hidalgo, P., Herrault, F., Glezer, A., Allen, A., Kaslusky, S., and St. Rock, B., "Heat Transfer Enhancement in High-Power Heat Sinks using Active Reed Technology," THERMINIC, Barcelona, Spain, October, 2010.
  29. Huang, W., Shin, S.J. and Sung, H.J., "Simulation of flexible filaments in a uniform flow by the immersed boundary method," *J. Comput. Phys.*, **226**, 2206-2228, 2007.
  30. Incropera, F.P., DeWitt, D.P., Bergman, T.L., and Lavine, A.S. "Fundamentals of Heat and Mass Transfer," John Wiley and Sons, 6th Edition, 2007.
  31. Incropera, F.P., DeWitt, D.P., Bergman, T.L., Lavine A.S., *Fundamentals of Heat and Mass Transfer*, John Wiley and Sons, 6th Edition, 2007.
  32. Jones, M.A., "The separated flow of an inviscid fluid around a moving flat plate," *J. Fluid Mech.*, **496**:405–401, 2003.
  33. Kim, S., Huang, W.-X. and Sung, H.J., "Constructive and Destructive Interaction Modes between Two Tandem Flexible Flags in Viscous Flow," *Journal of Fluid Mechanics*, **661** 511-521, 2010.
  34. Kornecki, A., Dowell, E. H. and O'Brien, J. On The Aeroelastic Instability of Two-Dimensional Panels in Uniform Incompressible Flow," *J. Sound Vib.* **47**, 163-178, 1976s.
  35. Krasny, R. "Vortex Sheet Computations: Roll-Up, Wakes, Separation," *Lectures in Applied Mathematics*, **28**:385–402, 1991.
  36. Leonard, B., "Simple high-accuracy resolution program for convective modelling of discontinuities," *Int. J Numer. Methods Fluids.*, **8**, 1291-1318, 1988.
  37. Mahalingam, R., and Glezer, A., "Design and Thermal Characteristics of a Synthetic Jet Ejector Heat Sink", *Journal of Electronic Packaging*, **127**, 172, 2005.
  38. Mahefkey, T., Yerkes, K., Donovan, B., and Ramalingam, M., "Thermal Management Challenges For Future Military Aircraft Power Systems," SAE Technical Paper 2004-01-3204, 2004, doi:10.4271/2004-01-3204.

39. Mahmood, G. I., Sabbagh, M. Z., and Ligrani, P. M. "Heat Transfer in a Channel with Dimples and Protrusions on Opposite Walls, *J. Thermophysics and Heat Transfer*, **15**, No.3 275-283, 2001.
40. Maniyeri, R. and Kang, S., "Numerical study on bacterial flagellar bundling and tumbling in a viscous fluid using an immersed boundary method," *Appl. Math Model.*, **38**, 3567-3590 2014.
41. Mittal, R. Dong, H. Bozkurtas, M. Najjar, F.M. Vargas, A. and von Loebbecke, A., "A Versatile Sharp Interface Immersed Boundary Method For Incompressible Flows With Complex Boundaries," *J. Comp.Phys.*, **227**, 2008.
42. Mittal, R., Iaccarino, G. "Immersed Boundary Methods," *Annual Review of Fluid Mechanics*, **37**:239-61, 2005
43. Nitsche, M. and Krasny, R., "A numerical study of vortex ring formation at the edge of a circular tube," *J. Fluid Mech.*, **276**:139–161, 1994.
44. Ozceyhan, V., Gunes, S., Buyukalaca, O. and Altuntop, N., "Heat transfer enhancement in a tube using circular cross sectional rings separated from wall," *Appl Energy*. **85**, 988-1001 (2008).
45. Pan, T. Joseph, D., Bai, R., Glowinski, R. and Sarin, V., "Fluidization of 1204 spheres: Simulation and experiment," *J. Fluid Mech.*, **451**, 169-191, 2002.
46. Peskin, C.S., "The immersed boundary method," *Acta Numerica.*, **11**, 2002.
47. Promvonge, P., Chompookham, T., Kwankaomeng, S. and Thianpong, C., "Enhanced heat transfer in a triangular ribbed channel with longitudinal vortex generators," *Energy Conversion and Management*. **51**, 1242-1249, 2010.
48. Seo J. H. and Mittal, R. "A sharp interface immersed boundary method with improved mass conservation and reduced spurious pressure oscillations", *Journal of Computational Physics*, **230**(19), 7347-7363, 2011.
49. Shelley M. J. and Zhang J., "Flapping and Bending Bodies Interacting with Fluid Flows," *Annu. Rev. Fluid Mech.*, **43**, 449–465, 2011.
50. Shoele, K. and Zhu Q., "Leading edge strengthening and the propulsion performance of flexible ray fins," *J. Fluid Mech.*, **693**, 402-432, 2012.
51. Shoele, K., and Mittal, R., "Computational study of flow-induced vibration of a reed in a channel and effect on convective heat transfer," *Physics of Fluids* (1994-present), **26** (12), 127103, 2014.
52. Shukla, R.K. and Eldredge, J.D., "An inviscid model for vortex shedding from a deforming body," *Theoretical and Computational Fluid Dynamics*, **21**(5):343–368, 2007.
53. Snyman, A. "Practical Mathematical Optimization: An Introduction to Basic Optimization Theory and Classical and New Gradient-Based Algorithms," *Springer*, 2005.
54. Stewart, S.E., and Strong, W.J., "Functional Model of a Simplified Clarinet," *J. Acoust. Soc. Am.*, **68**, 109-120, 1980.
55. Tanaka, T., M. Itoh, et al. "Influence of inclination angle, attack angle, and arrangement of rectangular vortex generators on heat transfer performance." *Heat Transfer - Asian Research* **32**(3): 253, 2003.
56. Theodorsen, T., "General Theory of Aerodynamic Instability and the Mechanism of Flutter," NACA Tech. Rep. TR-496, 1935.



57. Tiggelbeck, S., N. K. Mitra, et al. "Flow structure and heat transfer in a channel with multiple longitudinal vortex generators." American Society of Mechanical Engineers, Heat Transfer Division, (Publication) HTD, Atlanta, GA, Publ by ASME, New York, NY **182**: 79, 1991.
58. Tornberg, A. and Shelley, M.J., "Simulating the dynamics and interactions of flexible fibers in stokes flows," *J. Comput. Phys.*, **196**, 8-40, 2004.
59. Tsia, J. and Hwang, J., "Measurements of heat transfer and fluid flow in a rectangular duct with alternate attached-detached rib-arrays," *Int. J. Heat Mass Transfer.*, **42**, 2071-2083, 1998.
60. Turek, S., Hron, J., "Proposal for numerical benchmarking of fluid-structure interaction between an elastic object and laminar incompressible flow", *Springer*, 2006.
61. Uddin, E., Huang, W. and Sung, H.J., "Interaction modes of multiple flexible flags in a uniform flow," *J. Fluid Mech.*, **729**, 563-583, 2013.
62. Uhlmann, M., "An immersed boundary method with direct forcing for the simulation of particulate flows," *J. Comput. Phys.*, **209**, 448-476, 2005.
63. United States Air Force Scientific Advisory Board, "Report on Thermal Management Solutions", Volume 2: Non-Proprietary Version ,*SAB-TR-07-05-NP*, August, 2007.
64. Von Kármán, T. and Burgers, J.M. "General aerodynamic theory – perfect fluids," in *Aerodynamic theory*. Julius Springer, Berlin, 1935.
65. Vukasinovic, B., Rusak, Z., and Glezer, A., "Dissipative, Small-Scale Actuation of a Turbulent Shear Layer," *J. Fluid Mech.*, **656**, 51 -81, 2010.
66. Wang, S. K. Hung, T. C. Lin G. W. & Pei B. S., "Numerical Simulations for the Phenomena of Vortex-Induced Vibration and Heat Transfer of a Circular Cylinder," *Numerical Heat Transfer*, Part A: Applications, **45**:7, 719-736, 2004.
67. Wang, X. "A Numerical Study of Vorticity-Enhanced Heat Transfer," Georgia Tech, 2014.
68. Wang, Z., Fan, J. and Luo, K., "Combined multi-direct forcing and immersed boundary method for simulating flows with moving particles," *Int. J. Multiphase Flow.*, **34**, 283-302, 2008.
69. Wiltse, J. M., and Glezer, A. "Direct excitation of Small-Scale Motions in Free Shear Flows," *Physics of Fluids*, **10**, 2026-2036, 1998.
70. Xu, G., Guenin, B. and Vogel, M. "Extension for High Power Processors," *The Ninth Intersociety Conference on Thermal and Thermomechanical Phenomena in Electronic Systems. ITherm '04*. 186-193, 2004.
71. Zerby, M. and Kuszewski, M. "Final report on next generation thermal management (NGTM) for power electronics," NSWCCD Technical Report TR-82-2002012, 2002.

# AFOSR Deliverables Submission Survey

Response ID:6613 Data

1.

## 1. Report Type

Final Report

## Primary Contact E-mail

Contact email if there is a problem with the report.

ari.glezer@me.gatech.edu

## Primary Contact Phone Number

Contact phone number if there is a problem with the report

404-894-3266

## Organization / Institution name

Georgia Institute of Technology

## Grant/Contract Title

The full title of the funded effort.

Enhanced Forced Convection Heat Transfer using Small-Scale Vorticity Concentrations Effected by Flow-Driven, Aeroelastically Vibrating Reeds

## Grant/Contract Number

AFOSR assigned control number. It must begin with "FA9550" or "F49620" or "FA2386".

FA9550-13-1-0053

## Principal Investigator Name

The full name of the principal investigator on the grant or contract.

Ari Glezer

## Program Manager

The AFOSR Program Manager currently assigned to the award

Dr. Douglas R. Smith

## Reporting Period Start Date

05/01/2013

## Reporting Period End Date

04/30/2016

## Abstract

The three-year joint experimental, modeling, and numerical research program focused on the formation, shedding, and advection of a hierarchy of small-scale vortical motions induced by autonomous, aeroelastic fluttering of a planar thin-film reed that is cantilevered in the center plane of a rectangular air channel. The program built on complementary capabilities of experiments and models to explore the flow mechanisms and scaling of the interactions between the reeds and the channel flow, and develop the fundamental knowledge needed to exploit flow, structure, and heat transfer interactions to overcome the limits of forced convection heat transport from conventional air-side heat exchangers at low (laminar or transitional) Reynolds numbers. Nonlinear vortex-sheet simulations were used to determine the unstable range of the inviscid channel flow is to the reed's flapping motions, and showed that for heavier reeds, greater confinement expands the domain of instability and leads to higher flapping modes at critical channel widths. Simulations using coupled flow-structure-thermal models and immersed boundary-based solver for 2- and 3-D configurations provided insight into the reed-enhanced heat transfer. Measurement techniques were developed to capture the nominally time-periodic interactions of the reed with the channel flow along

DISTRIBUTION A: Distribution approved for public release.

with the spatial position of the reed's surface using high-resolution particle image velocimetry (PIV). Concave/convex surface undulations of the reed's structural vibration modes lead to formation and advection of vorticity concentrations and to alternate shedding of spanwise CW and CCW vortical structures that scale with the reed motion amplitude and channel width, and form motions of decreasing scales and enhanced dissipation that are reminiscent of a turbulent flow. The reed's impact on the surface is accompanied by transitory vorticity shedding and a local increase in the turbulent kinetic energy that result in strong enhancement of the heat transfer (the channel's thermal coefficient of performance is enhanced by 2.4-fold and 9-fold for base flow  $Re = 4,000$  and  $17,400$ , respectively, with corresponding decreases of 50 and 77% in the required channel flow rates). These improvements can be leveraged to enhance cooling rates or to reduce flows rates and/or the size of conventional heat sinks.

#### **Distribution Statement**

This is block 12 on the SF298 form.

Distribution A - Approved for Public Release

#### **Explanation for Distribution Statement**

If this is not approved for public release, please provide a short explanation. E.g., contains proprietary information.

#### **SF298 Form**

Please attach your SF298 form. A blank SF298 can be found [here](#). Please do not password protect or secure the PDF. The maximum file size for an SF298 is 50MB.

[sf298 final.pdf](#)

**Upload the Report Document. File must be a PDF. Please do not password protect or secure the PDF. The maximum file size for the Report Document is 50MB.**

[AFOSR FA9550-13-1-0053 Final Report Georgia Tech Johns Hopkins U Michigan.pdf](#)

**Upload a Report Document, if any. The maximum file size for the Report Document is 50MB.**

#### **Archival Publications (published) during reporting period:**

Alben, S., "Flag Flutter in Inviscid Channel Flow," Phys. Fluids, 27, 033603, 2015.

Hidalgo, P. and Glezer, A., "Small-Scale Vorticity Induced by a Self-Oscillating Fluttering Reed for Heat Transfer Augmentation in Air Cooled Heat Sinks", ASME 2015 InterPACK Conference, San Francisco, CA, July 2015.

Hidalgo, P. Jha, S., K., and Glezer, A., "Enhanced Heat Transfer in Air Cooled Heat Sinks using Aeroelastically Fluttering Reeds," 21st International Workshop on Thermal Investigations of ICs and Systems, Paris France, September, 2015.

Jha, S., K., and Glezer, A. "Direct Excitation of Small Scale Motions for Enhancement of Heat Transfer in Transitional Channel Flow using an Autonomous Aeroelastically Vibrating Reed," in preparation for submission to the Journal of Fluid Mechanics.

Shoele, K., Mittal, R., "Computational Study of Flow-Induced Vibration of a Reed on a Channel and Effect on Convective Heat Transfer," Phys Fluids, 26: 127103, 2014.

Shoele, K., Mittal, R., "Flutter Instability of a Thin Flexible Plate in a Channel," J. Fluid Mech., 786, 29-46, 2016.

Shoele, K., Glezer, A., and Mittal, R., "Enhancement of Convective Heat Transfer in a Micro-Channel using Flexible Self-Oscillating Reeds," 17th USNCTAM, Michigan, 2014.

#### **2. New discoveries, inventions, or patent disclosures:**

**Do you have any discoveries, inventions, or patent disclosures to report for this period?**

No

**Please describe and include any notable dates**

**Do you plan to pursue a claim for personal or organizational intellectual property?**

**Changes in research objectives (if any):**

**Change in AFOSR Program Manager, if any:**

**Extensions granted or milestones slipped, if any:**

DISTRIBUTION A: Distribution approved for public release.

**AFOSR LRIR Number**

**LRIR Title**

**Reporting Period**

**Laboratory Task Manager**

**Program Officer**

**Research Objectives**

**Technical Summary**

**Funding Summary by Cost Category (by FY, \$K)**

	Starting FY	FY+1	FY+2
Salary			
Equipment/Facilities			
Supplies			
Total			

**Report Document**

**Report Document - Text Analysis**

**Report Document - Text Analysis**

**Appendix Documents**

**2. Thank You**

**E-mail user**

Jul 30, 2016 09:41:31 Success: Email Sent to: ari.glezer@me.gatech.edu